# NON-INVASIVE, MULTI-MODAL SENSING TECHNIQUES FOR DETECTING INFILTRATION DURING INTRAVENOUS THERAPY

A Thesis
Presented to
The Academic Faculty

by

Jambu A. Jambulingam

In Partial Fulfillment
of the Requirements for the Degree
Master of Science in the
School of Electrical and Computer Engineering

Georgia Institute of Technology
December 2015

Copyright © 2015 by Jambu A. Jambulingam

# NON-INVASIVE, MULTI-MODAL SENSING TECHNIQUES FOR DETECTING INFILTRATION DURING INTRAVENOUS THERAPY

Approved by:

Professor Omer T Inan, Advisor
School of Electrical and Computer Engineering
*Georgia Institute of Technology*

Professor Jennifer O Hasler
School of Electrical and Computer Engineering
*Georgia Institute of Technology*

Professor Hua Wang
School of Electrical and Computer Engineering
*Georgia Institute of Technology*

Date Approved: 1 December 2015

# ACKNOWLEDGEMENTS

I would like to express my sincere gratitude to my advisor, Dr. Omer T. Inan, for his continuous support and guidance. His passion for medical research and knowledge of electronics has been my primary source of inspiration during my wonderful time at Georgia Tech.

I would like to acknowledge Dr. Jennifer O. Hasler and Dr. Hua Wang for their time and consideration by serving on my thesis committee. I would like to acknowledge Russell S. McCrory, Leanne L. West, and Lynn Pogue for their contributions to this work. I would also like to acknowledge Children's Healthcare of Atlanta and the Center for Transforming Pediatric Healthcare Delivery at Georgia Tech for their funding contributions. I would like to acknowledge my fellow students in the Inan Research Lab and my friends who have supported me in all facets of studies and life.

Lastly, my family provided me with unconditional love and encouragement as always. To them, I am extremely grateful.

# TABLE OF CONTENTS

# LIST OF TABLES

# LIST OF FIGURES

# SUMMARY

Intravenous infiltration is a condition wherein an infused solution leaks inadvertently into soft tissue surrounding a hypodermic needle site. This occurrence affects over 10% of patients in hospitals worldwide, and can lead to severe tissue damage if not treated immediately. However, the methods currently used by medical staff to detect an infiltration are subjective and prone to error. Infiltration becomes an even larger concern in the neonatal intensive care unit, where neonates have a much higher probability of infiltration due to having smaller veins. Unfortunately, infiltrations mostly go unnoticed for an extended period of time due to the neonate's inability to communicate with medical staff. For these reasons, automatic IV infiltration detection could greatly reduce the risk associated with this damaging condition. This dissertation proposes a novel design that uses non-invasive sensing in conjunction with a low-power embedded computing platform to deliver continuous infiltration monitoring around the IV catheter site. This kind of system could be able to detect an infiltration by non-invasively monitoring for known symptoms: swelling of soft tissue, skin cooling, and increased skin firmness; these symptoms can be sensed by measuring skin stretch, temperature, and local bioimpedance. In addition, the system's low-power design and wireless capabilities make it ideal for continuous wear. The proposed automatic IV infiltration detection system could significantly improve the number of infiltrations identified and treated on time.

# CHAPTER I

# INTRODUCTION

Intravenous therapy, abbreviated as IV therapy, has proliferated through hospitals around the world as the primary method of delivering drugs, blood, and nutrition to patients. Today, over 90% of hospitalized patients undergo intravenous therapy, and it has become one of the primary tasks of hospital nursing staff; around 75% of a nurse's working time is spent administering IV therapy [23]. The use of intravenous therapy dates back to the 1600s, in a time which physicians used naturally occurring catheter to be able to access the human venous system [7]. The practice progressed with the improving technology behind catheter materials and insertion techniques, and was popularized during the world war era as a relatively simple and scalable method to deliver blood transfusions. In modern medical facilities, an IV angiocatheter can be successfully placed for a patient's drug or blood infusion in under three minutes.

However, the ease of this technique is counterbalanced with complications that nurses must to be carefully trained to handle. Of the many complications that exist, IV infiltration, or the inadvertent leakage of a nonvesicant solution into surrounding tissue, is one of the most common incidents that coincidentally has the most severe consequences as well. Though the term Extravasation is associated with the leakage of a vesicant solution into surrounding tissue, this thesis considers both conditions under the term Infiltration. IV infiltration can occur because of an imperfect mechanical placement of the catheter, excessive movement by the patient, or due to pharmaceutical effects of the solution being used. The resulting effects of an IV infiltration are based on the pharmalogical characteristics of the solution being administered, but common side effects are skin loss, muscle and tendon necrosis, scarring, and regional

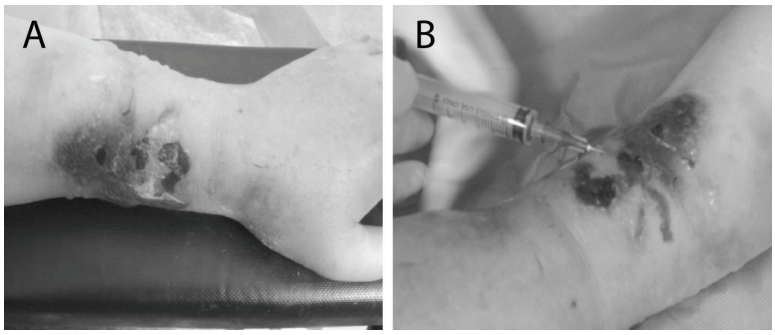


**Figure 1:** Images showing a patient with IV infiltration: A) Left forearm edema formation around catheter site identified after 20 minutes of IV therapy administration of 600 ml saline solution and 50 ml red blood cells B) Injecting hyaluronidase into forearm as an antibiotic after identification of infiltrated solution. Images used under Creative Commons Attribution License [43].

pain (Fig. 1) [15, 1]. While there are treatments that can be administered to alleviate these side effects, the most difficult part of the treatment is to detect the infiltration in a timely manner.

Currently IV infiltration is detected either by a nurse witnessing the symptoms first hand, or by the patient alerting medical staff of any symptoms. However, when the patient is unable to communicate, or when the nurse does not have a clear line of sight to the IV catheter site, it becomes nearly impossible to detect an infiltration. This is often the case when the patient is under anesthesia, undergoing surgery and draped, or otherwise unable to communicate (Fig. 3) [38]. Detecting IV Infiltration among infants comes with greater difficulty, who are not be able to clearly communicate with the nursing staff. Since the nurses in pediatric care are handling the needs of many infants at any given time, it becomes difficult for the nurse to identify an infiltration in a short time (Fig. 2) [49]. Monitoring infants in the Neonatal Intensive Care Unit (NICU) is critical, and a complication like this can easily turn around the health of an otherwise healthy infant.

There have been a few attempts to design automated IV infiltration detection devices, including one that uses an optical sensor to monitor the site of the IV catheter [52]. The device is able to detect when an infiltration occurred, but the cost and

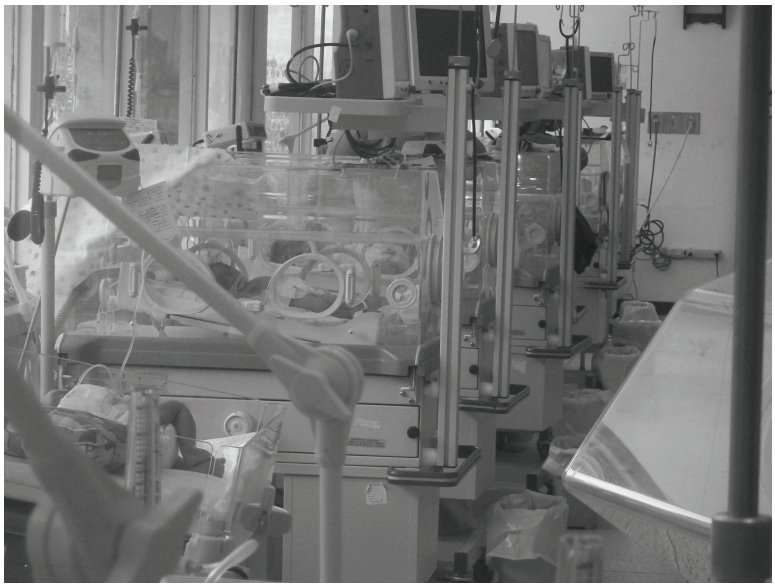

**Figure 2:** A Neonatal Intensive Care Unit (NICU) at a hospital. Neonates are placed in isolettes to maintain environmental conditions suitable for the newborn. The IV catheter is placed for the infant via inside the isolette alongside other equipment being used for ventilation and climate control. Image used under GNU Free Documentation License [12].

bulkiness of the optical sensing device makes this technique infeasible, aside from the motion artifacts and illumination requirements the device has. Mounting this complex rig on an infant poses an even greater challenge. Ultimately, the system requirements for this implementation are too large of a burden for hospitals to use at scale.

## *1.1 Motivation*

The motivation behind this thesis is to design an automated IV infiltration detection device to reduce the risk of an infiltration, by giving medical staff enough time to respond with the appropriate treatment. The automated detection of IV infiltration has to be simple enough to be able to scale, but also be robust enough to differentiate between infiltration and noise artifacts. The best way to accomplish these goals was to create a embedded system device that had sensing capabilities onboard. By understanding the symptoms that arise from infiltration, a sensing scheme was created to detect each symptom before confirming whether an infiltration has occurred. The

**Figure 3:** A typical surgery environment with extensive draping over the patient. Progressive stages of draping allow the surgeons access only to sites of interest, but impede the view of the rest of the body. Medical staff has little to no line-of-site vision of the IV catheter site being used. Image used under Creative Commons CC0 License [37].

non-invasive symptoms of IV infiltration that can be measured are the swelling of soft tissue, skin cooling, and increased skin firmness [11]. By using low power sensors and electronics, the sensing device would be able to stay attached to the body and communicate with medical staff devices wirelessly.

## *1.2 Sensing Modalities*

Skin cooling occurs due to the release of cooler liquid around the catheter site after an infiltration. To monitor this, a simple temperature sensor can be used on the skin. However, to improve the response time of the device alerting medical staff about an infiltration, an increased resolution would allow the device to check other parameters after a quick temperature change is detected. By using two Resistance Temperature Detectors, or RTDs, one placed away from the catheter site as a skin temperature reference and one placed near the catheter site, detecting the differential temperature can inform the nurses whether a threshold has been reached. By using very precise RTDs designed for interfacing to human skin, the device can achieve

a 0.1°C resolution. The RTD is read using analog circuitry and processed by a microprocessor using an analog-to-digital converter. This circuitry is designed to use the full range of the ADC to measure temperatures between 0°C and 50°C, and with skin temperature resting at around 37°C, this results in both a wide range and a fine resolution to detect infiltration with.

The swelling of soft tissue can be modeled as a ballooning of the skin surrounding the IV catheter. The fluid leaking into the surrounding soft tissue causes the skin to expand radially. To sense this swelling, a network of strain gages are placed around the IV catheter site. Strain gages can be used to detect deflection, and their resistance changes slightly based on the degree of strain applied. By placing the strain gages equidistant around the catheter site, the device is able to capture skin swelling in all directions surrounding the vein of interest. Since a strain gages sensitivity is affected negatively by changing temperatures, the use of a full bridge circuit ensures that the device would negate the effects of temperature [31]. The selection of a strain gage was also influenced by this temperature dependency, thus it was decided to use temperature-compensated strain gages with a 0.6%/°C temperature coefficient and a range from 0°C to 100°C. Texas Instrumentss AFE4300 analog front-end contains a Wheatstone bridge input with a serial-peripheral interface (SPI), and the results can be captured and streamed to a host device.

Increased skin firmness can be captured by measuring the change in bioelectrical impedance in the area surrounding the IV catheter. Known as bioimpedance, this technique uses a small, safe alternating electrical current to measure a potential difference between two electrodes placed on the body. Using bioimpedance can allow us to decipher the body composition in a target area, and a localized increase in conductive IV fluids can reduce the measured impedance [50]. This measured impedance can be modeled to be a network of resistors and capacitors. By understanding these values, we can measure the varying firmness of skin in the locations around the catheter to

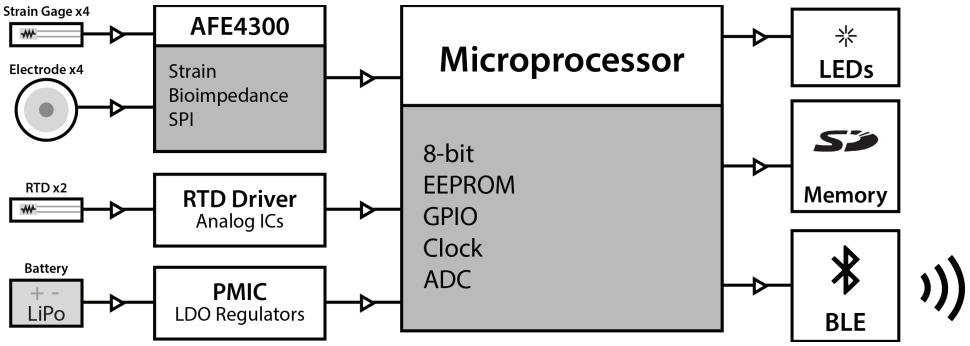


**Figure 4:** System Architecture of non-invasive automated IV Infiltration detection device. The current iteration of the system places the peripheral sensors on the body with the microprocessor and communications off-body. Future designs of this device are intended to be in an all-encompassing mechanical structure placed near the IV catheter site.

identify an infiltration. TIs AFE4300 computes bioimpedance using the four wire model of measuring voltage on two separate electrodes near which the current was passed, and it has an SPI interface to read voltage from the electrodes. The passive network model shown below from Webster is valid for using gel electrodes, which ensures firm skin contact [50].

A microprocessor is used to bring all of these sensors together, with enough on-board computing power to collect and send this data to a host computer for processing. The collected data is stored on an on-board secure digital (SD) card, which acts as a local hard drive. This data is also streamed in packets to a host computer over Bluetooth, which can then be used with a plotting tool such as MATLAB to visualize the data. The system architecture in Figure 4 outlines how the sensing circuits, microprocessor, wireless, memory, and general-purpose inputs/outputs (GPIOs) work to detect infiltration.

## *1.3 Custom Electronics*

The described sensing technologies were first characterized independently using evaluation hardware and software. The choice of sensors to be used for this device were based on our technical specifications of temperature and bioimpedance, and also based

on the wireless and power capabilities of the device. The TI AFE4300 bioimpedance and strain gage front end is used alongside custom analog RTD circuitry, and an Atmel microprocessor controls the inputs and outputs of the device. After prototyping this system on the breadboard level, the first revision of the printed circuit board (PCB) was manufactured to facilitate testing and firmware development. This board, show in Figure 5, would be placed near the patients arm, with the sensors coming off the board and interfacing with the patient. The sensors are placed on the patient arm for capturing data, and removed when an IV catheter needs to be reoriented. While the goal of the device would be to miniaturize the electronics to fit on the arm, this initial prototype abstracted the mechanical fixtures necessary and requires placing all computing electronics off the body. After writing the firmware, we are able to read values directly from these sensors and write the raw data to an SD card. The firmware also supports data transfer using the onboard Bluetooth module to a serial port on a host device.

A second iteration of the PCB was designed to add new functionality and reduce complexity in debugging. Additionally, a mechanical housing was made to contain the PCB and allow access to the sensor interfaces and other access interfaces. Figure 6 shows the second revision circuit board housed in a 3D printed and acrylic form factor. With these electronics designed, the automated intravenous detection system can begin to be tested for further characterization of the sensing modalities and to understand better the biosignal relevance of infiltration symptoms.

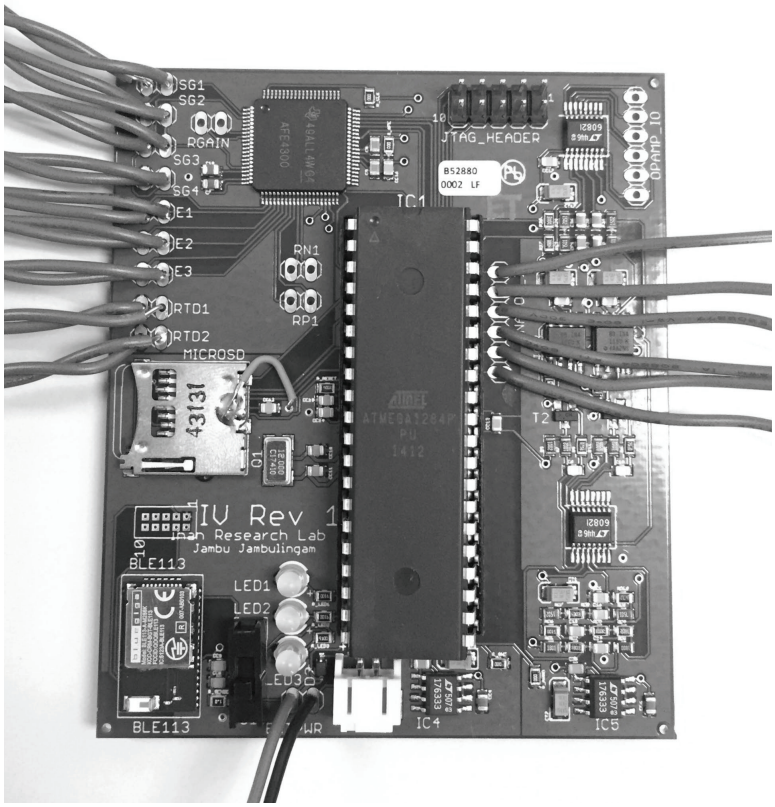


**Figure 5:** IV Rev 1 printed circuit board with break out connections for sensors to be placed on the body. The board measures 2.9"x3.3"x2mm (WxLxH).


**Figure 6:** IV Rev 2 printed circuit board with mechanical form factor for off-body use. This board and housing designed to begin to testing this system on the bench-top and to begin human trials. The board measures 2.8"x3.3"x2mm (WxLxH).

# CHAPTER II

# BACKGROUND

Intravenous (IV) therapy is a simple and effective way to access the venous system; however, there are inherent risks associated with interfacing an IV catheter with the body. While biocompatability, liquid content, and sterilization are commonly mentioned risks, this thesis focuses on the risks associated with the mechanical placement of the IV catheter. This chapter will present all necessary background information to understand IV therapy, catheter infiltration, and the sensing techniques that will be used for the automatic detection of an infiltration.

## *2.1 Intravenous Therapy*

Intravenous therapy has been one of the most common medical procedures since its invention in the 17th century. It provides physicians a method to access a patient's venous system for safe infusion of medication, hydration fluid, blood product, or nutritional supplement [17]. This technique is used to administer therapies in the case where alternate administration is less effective or when it is the only method available. Between 60-90% of hospitalized patients undergo IV therapy, and over 300 million peripheral catheters are used each year in the United States alone. IV therapy has a wide range of applications: it can be used for hydration in severely dehydrated patients, nutrition in patients with severe metabolic conditions, or for delivering blood to patients experiencing cardiac dysfunction.

IV therapy is used to interface with the central and peripheral venous systems, which contain arteries, veins, and capillaries throughout the entire body. These vessels facilitate blood flow to and from the heart to allow for perfusion and ventilation of body tissue. Figure 7 highlights the veins that are most commonly used for IV therapy

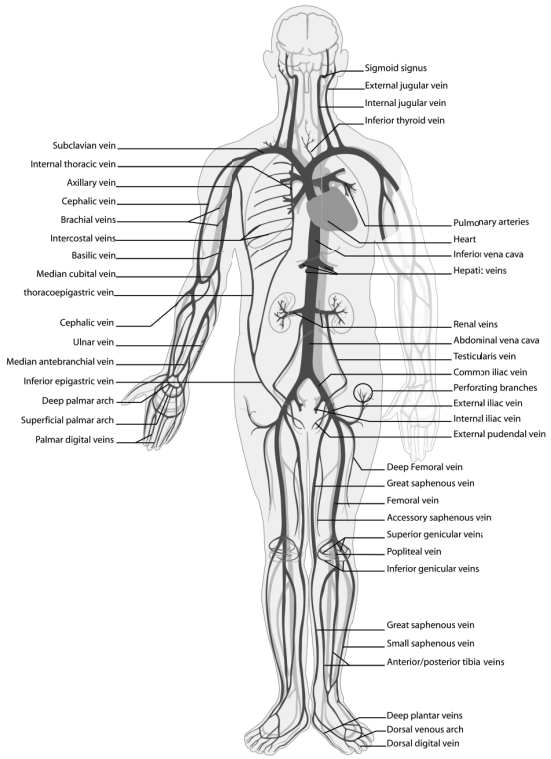


**Figure 7:** Illustration showing central and peripheral venous system. The veins most commonly used for IV therapy are: Internal Jugular Vein, Femoral Vein, Cephalic Vein, Basilic Vein, Subclavian Vein. These sites can use either a non-tunneled, peripherally inserted, or midline catheter setup for venous infusion. Image used under GNU Free Documentation License [10, 13].

in both the central and peripheral venous system. The decision between using central or peripheral access depends primarily on the solution being administered. Peripheral veins are smaller and highly distendible, and hence can cause pain if solutions greater that 900mOsm/L are administered [10]. However, peripheral access is generally safer and easier to obtain, hence is preferred if the solution can be infused in low volume and osmolarity. The central venous system is primarily used for high volume infusion due to the size of accessible veins, and for patients whose peripheral venous catheter placement has low probability of success. It is also used when the solution being administered contains vasopressors that can lead to high risk of extravasation in smaller veins [17].

**Table 1:** Percentage Composition of TPN Macronutrients Titrated in Water - based on data provided by [19]

| Macronutrient | Percentage of Solution |
|---|---|
| Protein (Amino Acid) | 15% |
| Carbohydrate (Dextrose) | 55-65% |
| Fat (Soybean or Safflower Oil) | 20-30% |

IV therapy can be administered for a delivering number of medications and hydration fluids, but this thesis focuses specifically on solutions used in pediatric care. Total parenteral nutrition (TPN) is a commonly used solution for infant nutrition in intensive care units, and consists of the ingredients listed in Table 1. A more detailed composition is available in Appendix A. Around 2 liters of TPN is prepared per patient per dayDue to its high osmolarity and concentration of amino acids and dextose, TPN requires infusion through the central venous system's subclavian or internal jugular veins with high operator-dependent insertion risk [19]. Since it is generally advised to administer TPN using peripheral veins for short term infusion or for pediatric patients, the TPN must be infused with lipids (10-20%) to reduce the solution's osmolarity.

Pediatric patients in the neonatal intensive care unit (NICU) also commonly require the infusion of anesthetics, inotropic drugs, or antibiotics for continuous improvement of their health. An estimate of 12 mL/h of maintenance fluid is delivered to infants weighing 3-kg in the NICU, while infants with significant diseases can receive much more [3]. Some of the most used drugs in NICU's are listed in Table 2. The list of NICU drugs is accumulated from 220 hospitals in 32 states and Puerto Rico over a course of nine years [9]. These drugs are administered via IV therapy, which can pose a great risk if the aforementioned complications arise. An extensive list of drugs administered in NICU's is available in Appendix A.

**Table 2:** Most Commonly Reported Medications and Use Cases in NICU's - based on data provided by [9, 33]

| Medication | Use | Frequency |
|---|---|---|
| Ampicillin | Infection Treatment | 186,799 |
| Gentamicin | Gram Negative Bacteria Treatment | 171,388 |
| Vitamin (multivitamin) | Supplemental Feeding | 64,329 |
| Cefotaxime | Infection Treatment | 55,455 |
| Caffeine citrate | Apnea Treatment | 48,814 |
| Furosemide | Diuretic | 47,278 |
| Vancomycin | Gram Positive Bacteria Treatment | 44,218 |
| Dopamine | Blood Pressure Stimulant | 25,839 |
| Indomethacin (Ibuprofen) | Blood Vessel Constriction | 20,605 |
| Dexmethasone | Improved Lung Function | 20,398 |

The process for which an angiocatheter is placed for an infant is extremely complex, requiring the medical staff to follow guidelines very carefully. The equipment necessary for a successful intravenous catheter placement, known as venipuncture, is shown in Figure 8 [6]. Typically a 22-gauge angiocatheter (0.7176 mm outer diameter) is used to match the average diameter of an infant's peripheral veins. An anesthetic can be used locally 20-60 minutes prior to the venipuncture, to decrease the pain associated with the process [39]. It is extremely important to choose the correct site for venipuncture to prevent complications and ensure successful delivery of solutions. The most common site for infants is the antecubital fossa, the triangular area just under the anterior view of the elbow. The superficial dorsal vein, at the intersection above the palm and wrist, is also a commonly used site. Figure 9 shows all venous access sites used for infant venipuncture. However, infants whom are either very well nourished or dehydrated can both pose a challenge for a discovering a vein with enough diameter and blood flow for infusion.

Once the vein has been selected by the medical staff, a tourniqet must be applied proximal to the site to fill the vein with blood and make it easily identifiable. Then, the area must be cleansed with antiseptic to prevent any surface debris from infecting


**Figure 8:** Equipment required for IV catheter placement: tourniquet, antiseptic solution, sterile injection cap, non-sterile gloves, local anesthetics, catheter needle, gauze pads, syringe or angiocatheter tubing. Image used under Creative Commons Attribution License [36].

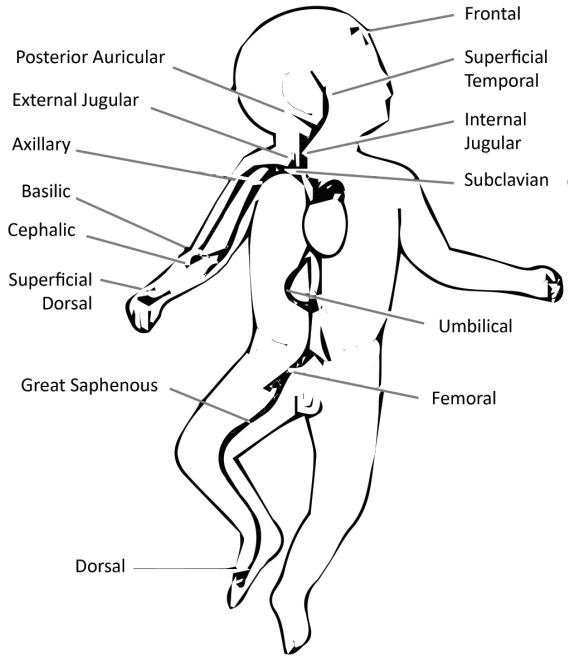


**Figure 9:** Venous access sites commonly used for neonates. The superficial dorsal vein is a primary site of interest for automated infiltration detection due to its distance from the shoulder and optimal device wear around the wrist. Image redrawn from [39].

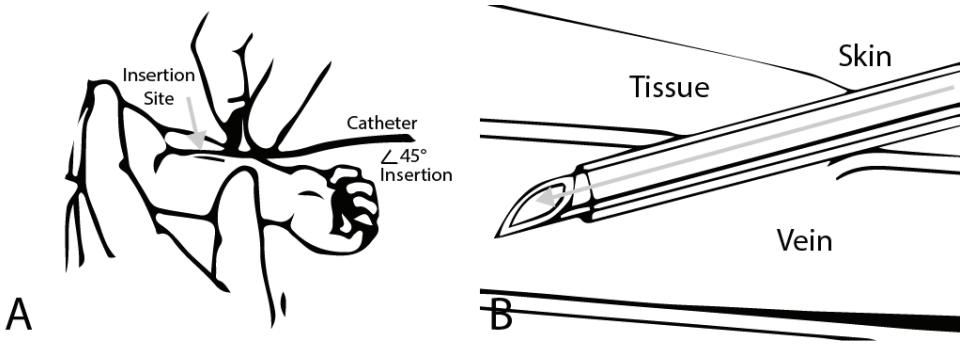


**Figure 10:** Antecubital venipuncture showing needle insertion A) at acute angle to the arm and B) approximately 1cm distal to the vein. If the needle is not inserted at the right angle or distance, the needle can rupture both walls of the vein and lead to edema formation. An IV infiltration will occur if IV therapy begins with the catheter attached to this site. Image redrawn from [6, 39].

the blood. When the area has dried, the vein can be straightened and stabilized. The thumb and middle finger can be placed around the vein to highlight the insertion location. Next, the needle must be applied at a 30 degree angle with respect to the arm, with the bevel side of the needle facing up (Fig 10). In a swift and smooth motion, the angiocatheter should be inserted about 1 cm distal to the vein. A successful venipuncture will cause a rapid flashback of blood, after which the angiocatheter's angle can be lowered parallel to the arm to insert it further into the vein. After the angiocatheter clicks into place, the tubing can be connected and IV therapy may begin.

The Center for Disease Control and Prevention has specified that IV catheters must be removed and replaced every 72 hours; therefore, it is no surprise that many complications can arise due to the complex procedure required for a successful venipuncture [20]. The IV catheter failure rate is between 35-50%. These failures can be related to phlebitis, infiltration, mechanical failure, dislodgement, or infection (Table 3). It is also important to note that the rate of failure rises as the catheter is repeatedly replaced [20]. Many providers find that the required 72 hour replacement of IV catheters is too long and end up replacing about 70% of them well before then. The median time of insertion is 84 hours, and an average of 1.7 catheters are required

**Table 3:** The 5 Modes of Peripheral IV Catheter Failure - based on data provided by [20]

| Mode of Failure | Range | Mean | Median |
|---|---|---|---|
| Phlebitis | 0.1%-63.3% | 15.4% | 9.0% |
| Infiltration | 15.7%-33.8% | 23.9% | 22.2% |
| Mechanical Failure | 2.5%-32.7% | 18.8% | 22.8% |
| Dislodgement | 3.7%-9.9% | 6.9% | 7.0% |
| Infection | 0.0%-0.44% | 0.2% | 0.2% |

per patient using IV therapy [20].

As found by Helm et. Al, the three components by which IV therapy fails are: *(1) the technology used, such as the catheter, connector, and dressing; (2) the caregiver technique applied, including all aspects of insertion, use, and care; and (3) and the bodys response to this technology and technique* [20]. With almost half of IV catheters failing amongst patients, the risks associated with IV usage rises greatly. Table 3 shows the mean occurrence as a percentage of patients that underwent IV therapy between 1990-2014, and the percentages of failures are extremely high. The most common failure listed, with a mean occurrence of 23.9%, is IV infiltration, the focus of this thesis. IV therapy and IV infiltration pose an even larger risk among infants, since their veins are much smaller and fragile [42].

IV infiltration is the accidental leakage of IV solution into the tissue surrounding the catheter site [18] . These conditions can have many consequences, from regional pain to potentially requiring surgical intervention. The most extreme cases of infiltration can result in long-term paralysis and eventual amputation. Nurses that administer IV therapy are required to be familiar with the IV solution being administered and the potential consequences if infiltration occurs. They are also required to check for common symptoms of infiltration, which include the following: *a) pain, tenderness, or discomfort b) edema at, above, or below the insertion site c) erythema at or above the insertion site d) blanching of the area around the insertion site e)*

*changes in the temperature of the surrounding skin f) numbness, tingling, or a feeling of "pins and needles" g) burning at the insertion site or along the venous path h) fluid leaking from the insertion site i) feeling of skin tightness around or below the insertion site j) bruising k) palpable cording of the vein* [18].

There are three main causes for IV infiltration. Firstly, mechanical problems with the fixation of the catheter can occur either during the venipuncture or the duration of the catheter inside the vein. During the venipuncture, the nurse handling the angiocatheter could have inserted deeper than the recommended 1 cm while maintaining the recommended 30°, causing the vein to rupture [39]. Also, patient movement either on or off the hospital bed can lead to the catheter tip puncturing the vein wall [18]. Secondly, a venous obstruction can cause an infiltration, for example a clot arising from disturbing other nearby veins. Thirdly, when multiple sites are punctured, the previously punctured sites can swell and cause a perturbation around the vein being used for infusion, thus leading to a possible infiltration. Inflammation can also be caused by other drugs being administered in the local area of venipuncture [18].

After an infiltration occurs, there are ways to treat the area, but the treatment's effectiveness is primarily based off the duration of the infiltration and whether the vesicant or nonvesicant being administered has a known antidote. If any of the aforementioned symptoms of an infiltration are noticed, the IV catheter must be removed as soon as possible. Next, a choice in antidote must be made based off of the solution. Phentolamine dosages of 5-10 mg diluted in saline have been used in the locally in the case of vasopressor extravasation. Another antidote used is Hyaluronidase, a protein enzyme that breaks down cellular structures in the surrounding tissues to rid of any administered drug attached [18]. Also, rapidly changing the temperature of the local area can induce vasodilation or vasoconstriction, allowing the medical staff to contain or spread the drug based on its known effects. Despite all of the mentioned antidotes, the most effective way to treat or prevent IV infiltration is to utilize a

better venipuncture and to respond quickly to any erroneous attempts, which this thesis discusses in a future chapter.

## *2.2 Bioimpedance*

Bioimpedance analysis (BIA) is a technique used to study the electrical properties of biological tissue as a means to monitoring body vitals and understanding disease prognosis. BIA has been studied since the late 18th century, and its original application was to estimate body fat composition, separating the mass of fat from the body's total water content [24]. But since than, the technique has been applied to help us understand much more about the human body. Bioimpedance at it's most fundamental level is defined as the ability of biological tissue to impede electricity [28]. While the body uses bioelectricity to provoke ionic activities on a intracellular level, this thesis considers the passive response of biological tissues when stimulated through an external current source. The benefit of using passive bioimpedance is that it provides researchers with a low-cost, noninvasive method to understand body tissue.

$$V = IR \tag{1}$$

Bioimpedance analysis rests of the basis of Ohm's law (Eq. 1). Georg Ohm announced his findings that *the currents furnished by different galvanic cells, or combinations of cells, are always directly proportional to the electromagnetic forces existing in the circuits in which the currents flow, and inversely proportional to the total resistances of these circuits* [30]. In the case of bioimpedence, Ohm's law is dependent on the frequency of the AC current applied, and thus can be represented as individual components of magnitude and phase angle (Eqs. 2,3,4). This separation of impedance magnitude and phase angle will become crucial when analyzing the real and reactive element models used to understand the body.

$$Z = R + jX_c \tag{2}$$

$$|Z| = \sqrt{R^2 + X_c^2} \tag{3}$$

$$\Phi = \arctan X_c/R \tag{4}$$

For a conductive material, the resistance is defined by its resistivity, measured in ohm-meters, and the geometry of the material. The geometry of the body is modeled best as a cylinder, which considers the height and the lean body mass of the subject (Fig. 11) [25]. The resistance that is analyzed using BIA is primarily due to the extracellular and intracellular fluids, but the cellular membrane itself is more appropriately modeled by reactance. The reactance of a conductive material is inversely related to the signal frequency and capacitance, and is shown in Eq. 5 [24].

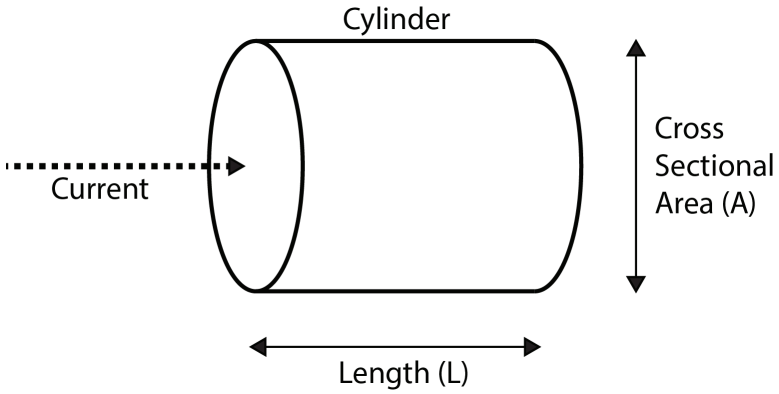


**Figure 11:** The geometry of the body modeled by an equivalent cylinder, with total resistance based on the dimensions of the cylinder: $R = \rho\frac{l}{A}$.

$$X_c = \frac{1}{2\pi * f * C} \tag{5}$$

The most commonly used circuit model of bioimpedance combines resistance and reactance in parallel. In Figure 12, $C_d$ represents the capacitance at the electrode-electrolyte interface, $R_d$ represents the leakage resistance at the same interface, and

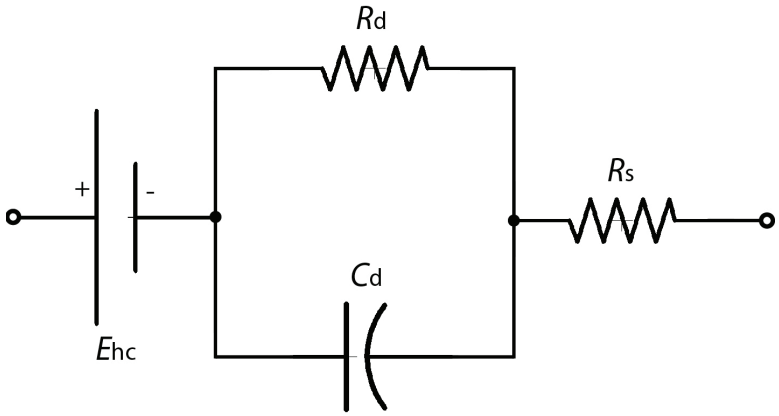


**Figure 12:** The RC network used to model the human body. The purely resistive path models the extracellular space of the body, while the reactive and resistive (mixed) path models the intracellular space of the body.

$R_s$ is the series resistance in the electrolyte itself. This circuit also illustrates how the interface model is frequency dependent. At low incident frequencies $1/\omega * C >> R_d$ , the purely resistive path is seen due to the AC blocking capacitor, and at high frequencies $1/\omega * C << R_d$ the resulting impedance is a combination of both $R_d$ and $R_s$ [50]. It is this behavior that allows researchers to use BIA to characterize tissues and how different medical conditions affect their composition.

To further describe the circuit model used for bioimpedance, we must also introduce a model for how the electrode interfaces with the skin. For this, the basic anatomy of skin must be reviewed. The skin is made of three layers: the epidermis, dermis, and subdermis (Fig. 13). The epidermis is the must crucial layer for measuring bioimpedance, as it is the outermost layer that is constantly being damaged and regrown [50]. New cells are constantly being created in the stratum germinativum, and they displace older damaged cells while propagating to the top of the epidermis. The constant flux between dead and new skin cells at the epidermis layer makes modeling this section over a long period of time very challenging. The bulk of the skin tissue is in the dermis layer, which also contains the nervous and vascular transports for the skin. Finally, the subdermis contains the sweat glands and ducts for skin perspiration. However, the dermis and subdermis do not have as much electrical

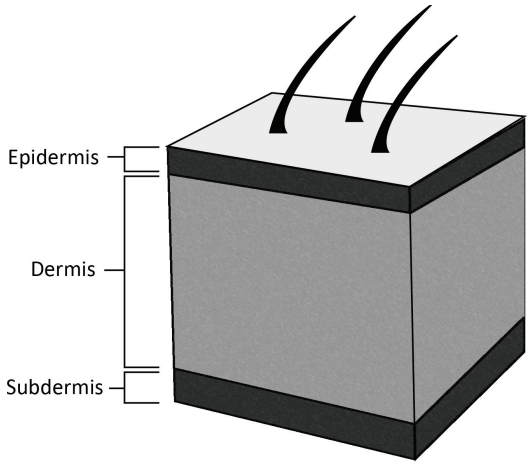


**Figure 13:** Cross-section diagram of skin with layers isolated. The blood vessels, follicles, oil glands, and sweat glands all reside in the dermis. The epidermis is the outermost layer that consists of melanocytes that make up the skin surface, and the subdermis contains fat and soft tissue giving skin its rigidity.

significant as the epidermal layer.

The electrode circuit model used is dependent on the type of electrode used for BIA. This thesis primarily considers variants of dry electrodes and metal-plate electrodes, which are made of a metallic conductor for skin contact and an electrolyte gel for establishing and maintaining skin contact (Fig. 14). Dry electrodes can be made of silver, copper, or other conductive materials. They provide a more comfortable way to measure bioimpedance, since there is no skin irritation from the use of any adhesive. However, securely mounting the dry electrodes to minimize noise artifacts can be challenging. In the case of gel-based electrodes, the chemical composition of the binding electrolyte can greatly change the intrinsic resistance and reactance. Table 4 shows some commonly used electrodes and their varying skin-electrode impedances. Typically, disposable electrodes use silver plating for skin contact and the contact layer is coated with AgCl, electrolyte, and an adhesive material. These electrodes have a snap on connector for the wiring to BIA current source, and meant to be easily placed on and removed from a patient.

The electrodes are excited with an alternating current (AC) current source, and

**Table 4:** Typical Real and Imaginary Impedance Values of Skin-Electrode Interfaces - based on data provided by [8]

| **Material** | $R_d$ | $C_d$ |
|---|---|---|
| Wet Ag/AgCl | 350kΩ | 25nF |
| Metal Plate | 1.3MΩ | 12nF |
| Thin Film | 550MΩ | 220pF |
| Cotton | 305MΩ | 34pF |
| MEMS | 650kΩ | - |

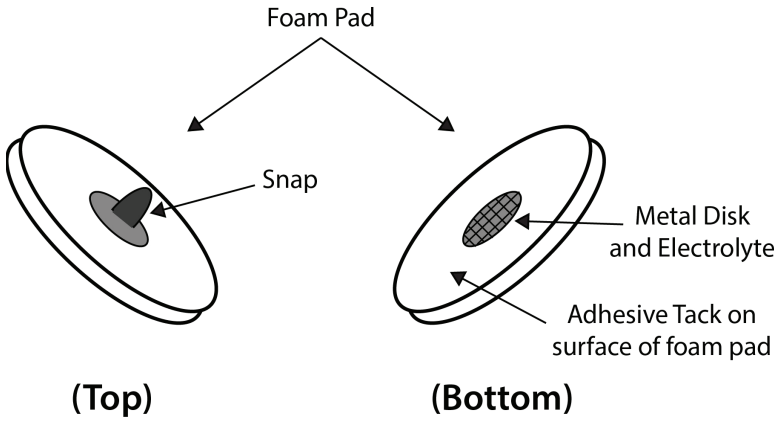


**Figure 14:** Diagram showing mechanical assembly of disposable metal-plate electrode with foam backing. The adhesive tack provides a strong connection for the electrode-skin interface, reducing the amount of motion artifacts present when taking bioimpedance measurements. The wet electrode is also well studied and has many proposed RC network equivalent models.

the frequencies of excitation are differentiated into two types of measurement: single frequency bioimpedance analysis (SF-BIA) and multiple frequency bioimpedance analysis (MF-BIA). SF-BIA, the most commonly used method, uses only 50kHz AC current and has been empirically characterized to calculate total body water and intracellular fluid content [24]. MF-BIA uses multiple frequencies (0, 1, 5, 50, 100, 200, and 500 kHz) to obtain total body water, intracellular and extracellular fluid content, and additionally fat free mass. It has been tested to be more accurate in intracellular and extracellular fluid contents, while SF-BIA more accurately calculates total body water. Both these measurements are used to calculate total body measurements, but localized BIA can be used to detect these quantities only in a specific area of the body [25]. The typical electrode placement for MF-BIA and SF-BIA are hand-to-foot, foot-to-foot, or hand-to-hand. For localized BIA, the placement of the BIA electrodes must be modified to target the local area, but can yield a better estimation of skeletal muscle mass.

The excitation current can be used in either a bipolar or tetrapolar electrode placement for BIA, however the tetrapolar measurement offers benefits that make it more accurate. The current needed for measuring bioimpedance is very low, typically a 64kHz AC current at $375\mu A_{RMS}$. As seen in Figure 15, bipolar measurements use the same pair of electrodes for both excitation and sensing. This method uses less electrodes, but it also measures the resistance of the electrode and wiring, which can be significant to up to 20% when measuring resistances under 1 k$\Omega$ [44]. This addition leads to adding more noise to the measurement than motion artifacts. Since the goal of BIA is to measure the impedance of the target skin-electrode interface and not the electrode's resistance itself, tetrapolar measurement proves to be a better measurement technique that neglects the electrode's resistance [4]. By using a two separate pairs of electrodes, one for excitation and one for sensing, the tetrapolar measurement senses the voltage directly at the electrode skin interface without driving

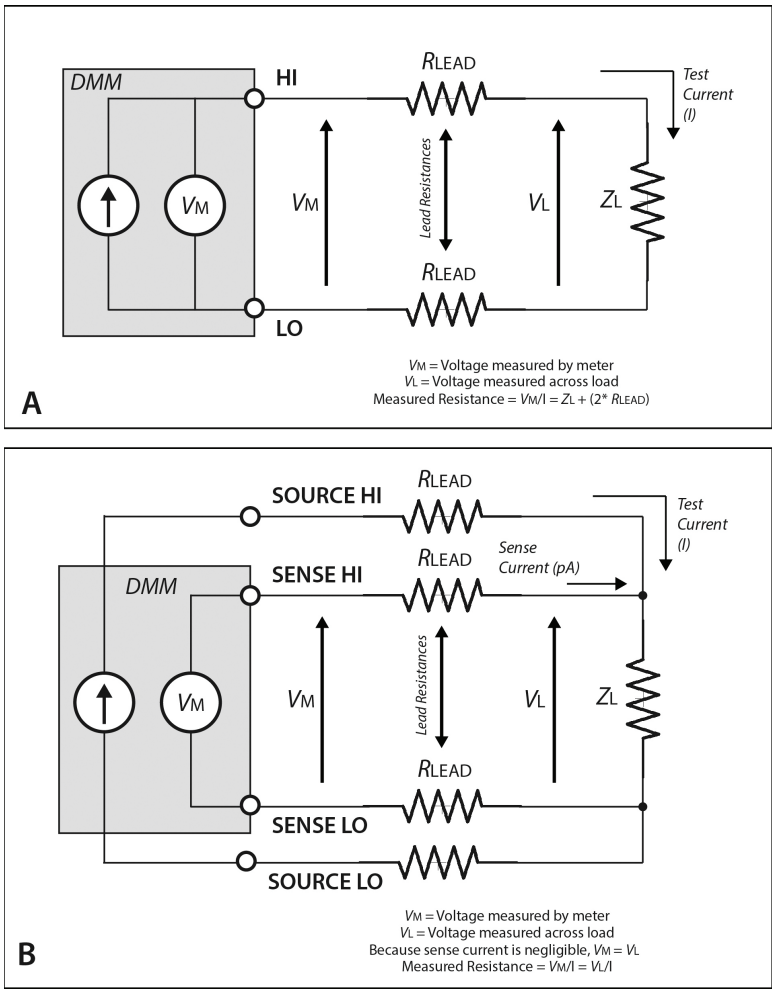


**Figure 15:** Comparison of circuit configurations for A) Two-Wire Resistance Measurement and B) Four-Wire (Tetrapolar) Measurement. The tetrapolar measurement requires four electrodes as opposed to the two required by two-wire measurement, and uses a larger test current ($\mu$A) and a smaller sense current (pA) to measure the load. In effect, the Lead resistances are neglected and only the load resistor is measured.

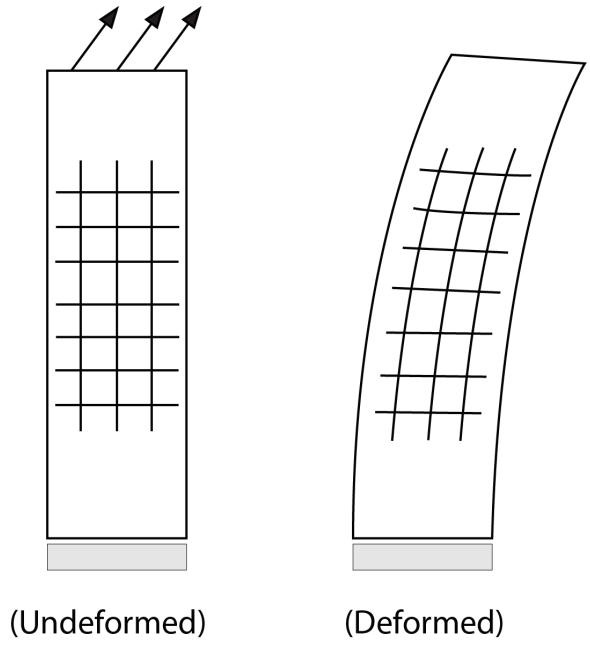


**Figure 16:** A rectangular cantilever beam deformed by an external force applied as shown with bold arrows. The center grid helps visualize the point-to-point deformation that leads to the bending of the rectangle.

current through the sense electrodes. This eliminates interface artifacts since there is negligible current flowing through the sense path, typically less than 100pA [44].

## *2.3 Material Deformation and Strain*

Material deformation and strain are introduced through the study of continuum mechanics as measurements of point-to-point displacement. Material deformation is based on the principle that elastic solids deform under external loading. This load is applied point-to-point, meaning that each point of the material is inhomogeneous in its deformation. A material can undergo many different kinds of deformation, including shearing and extension. Strain, the elastic deformation of interest, is defined as the change in relative displacements between points on a body [40]. Figure 16 shows a two-dimensional cantilever beam undergoing elastic deformation [40].

Strain can be geometrically modeled by a displacement vector of two positions. The vector is position and time dependent, as each point on a body can be deformed according to these parameters. Figure 17 shows strain in terms of the displacement

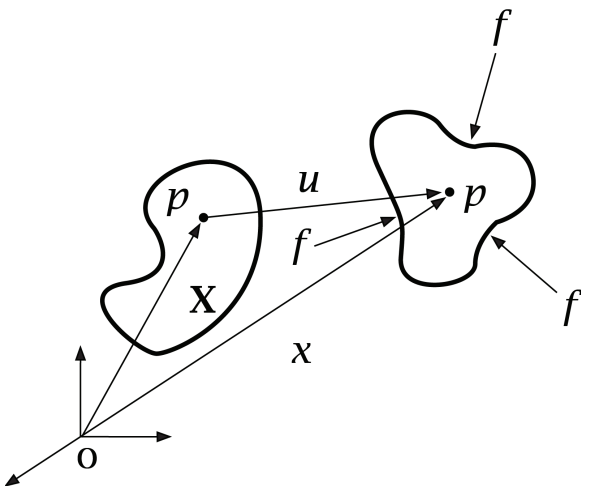


**Figure 17:** The displacement vector **u** shows the body's transformation at point P from the location of vector **X** to **x**. This is the trajectory by which the material deformation synthesis equations are based on.

vectors *u(X,t)* and *x(X,t)* [22]. The displacement vector equation and the vector applied to cartesian coordinates are shown in Equations 6 and 7. Dependent on which axes is used as the body's fixed support, the displacement may or may not differ from point to point on the x, y, or z axis.

$$\mathbf{u}(\mathbf{X}, t) = \mathbf{x}(\mathbf{X}, t) - \mathbf{X} \tag{6}$$

$$\mathbf{u} = u_x\hat{\mathbf{i}} + u_y\hat{\mathbf{j}} + u_z\hat{\mathbf{k}} \tag{7}$$

Many 20th century inventors had their own take on how to define stress mathematically, including Green and Lagrange, but for simplicity we will consider Green's definition of strain under the approximation of infinitesimal displacement ($x \sim X$ for $u_x$) [22]. We can define strain and shear as shown in Equation 8.

$$[\epsilon] = \begin{bmatrix} \epsilon_{xx} & \epsilon_{xy} & \epsilon_{xz} \\ \epsilon_{yx} & \epsilon_{yy} & \epsilon_{yz} \\ \epsilon_{zx} & \epsilon_{zy} & \epsilon_{zz} \end{bmatrix} \tag{8}$$

where

$$\begin{aligned}
\epsilon_{xx} &= \frac{\partial u_x}{\partial x}, \quad \epsilon_{xy} = \frac{1}{2}\left(\frac{\partial u_x}{\partial y} + \frac{\partial u_y}{\partial x}\right) = \epsilon_{yx} \\
\epsilon_{yy} &= \frac{\partial u_y}{\partial y}, \quad \epsilon_{yz} = \frac{1}{2}\left(\frac{\partial u_z}{\partial y} + \frac{\partial u_y}{\partial z}\right) = \epsilon_{zy} \\
\epsilon_{zz} &= \frac{\partial u_z}{\partial z}, \quad \epsilon_{xz} = \frac{1}{2}\left(\frac{\partial u_z}{\partial x} + \frac{\partial u_x}{\partial z}\right) = \epsilon_{zx}
\end{aligned} \tag{9}$$

On a cartesian coordinate plane, the angle of deformation from the origin of a point $(x, y, z)$ to the displaced point $(x', y', z'), \alpha$, is used to calculate the individual vector components of strain on the x-, y-, and z- axes [22]. The maximum and minimum strain that can be applied on a single axis (Eq. 10) occurs at the angle $\alpha = \alpha_p$ (Eq. 11).

$$\epsilon_{xx,max/min} = \epsilon_{yy,max/min} = \frac{\epsilon_{xx} + \epsilon_{yy}}{2} \pm \sqrt{\left(\frac{\epsilon_{xx} - \epsilon_{yy}}{2}\right)^2 + \epsilon_{xy}^2} \tag{10}$$

$$\alpha_p = \frac{1}{2}\tan^{-1}\left(\frac{\epsilon_{yy} - \epsilon_{xx}}{2\epsilon_{xy}}\right) \tag{11}$$

The next deformation that must be considered is beam bending. This thesis discusses strain and deformation for the ultimate use to detect skin expansion and contraction. If a small, square subsection of skin is used as the site of interest, a skin expansion perpendicular to this subsection can be modeled in the same way that a beam bends with a load applied orthogonally. Beam bending mechanics rests on enforcing equilibrium for the system; in other words, force and moment must be conserved (Eq. 12) [22].

$$\sum F_x = \sum F_y = \sum M_z = 0 \tag{12}$$

Figure 18 shows an initially straight beam that is deformed from the origin and illustrates what is expected during skin expansion [22]. The amount of skin expansion can be obtained by measuring the radius of curvature $\rho$. Before the deformation, $\overline{OB} = \Delta X$, and after, $\overline{OB} = \Delta\Theta(\rho - y)$, where $\Theta$ is the angle of curvature and y is the height of the line from the origin.

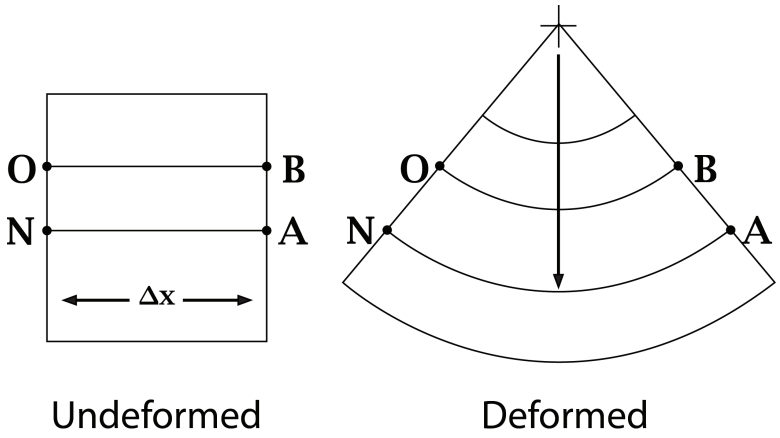


**Figure 18:** The initially straight beam is deformed by applying moment $M_z$ around the fixed center origin. $\overline{OB}$ and $\overline{NA}$ shows two different groups of points on a line that deform at a specific radius of curvature $\rho$.

As shown in Figure 18, a way to measure deformation is to mark points at a known starting location and monitor their displacement over the duration of the applied load. This is usually done by video, X-Ray, magnetic resonance imaging (MRI), or laser doppler [22]. However, strain gages, an invention made in the late 19th century, have proven to be the most reliable way to measure surface strain on structures. The strain gage is made of a long metallic wire that is patterned on a backing substrate (Fig. 19) [22]. Applying a mechanical load orthogonal to the direction of the metallic wire increases the total wire's impedance. The sensitivity of the sensing is based on the type of metal, type of backing, and the pattern that the wire is laid out in.

Strain gages need to be mounted axially to the structure of interest, and often offer very high resolution in measurements with small strain magnitudes. The small change in resistance needs to be amplified to output a relevant and measurable electrical value. The Wheatstone bridge has been used since the 19th century as a way to detect small changes in resistance, and today there are many more ways the circuit is used that what it was intended for. The basic Wheatstone bridge is made of four resistive elements, where one or more of them is a sensing element [31]. The Wheatstone bridge is able to respond to physical phenomena by converting the change in resistance of any of the legs into a change in voltage read across the bridge. More than one of the

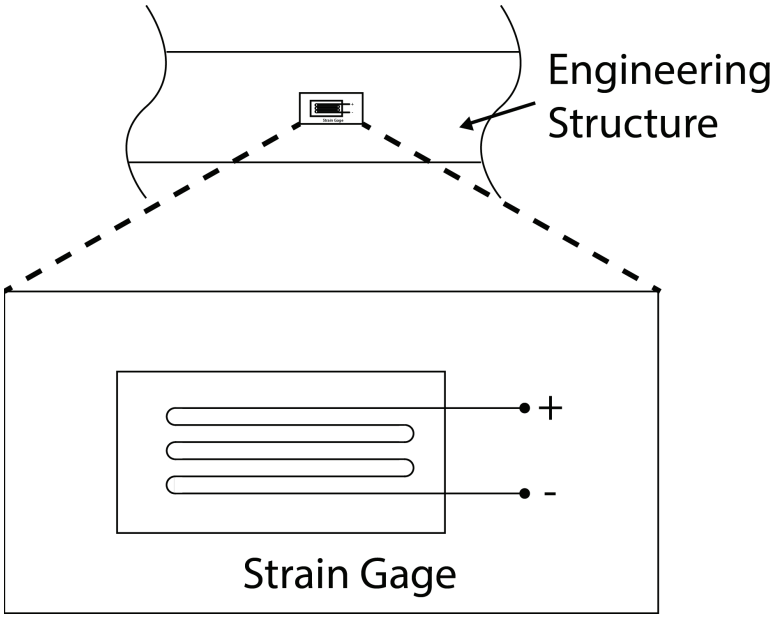


**Figure 19:** Diagram showing strain gage metallic wire, leads, and mounting structure. Strain gage's typical application are use on industrial metal substrates, such as rods or plates. However, the theory of operation still persists irrespective of the engineering structure used. Thus. the engineering structure for this application will be the human arm.

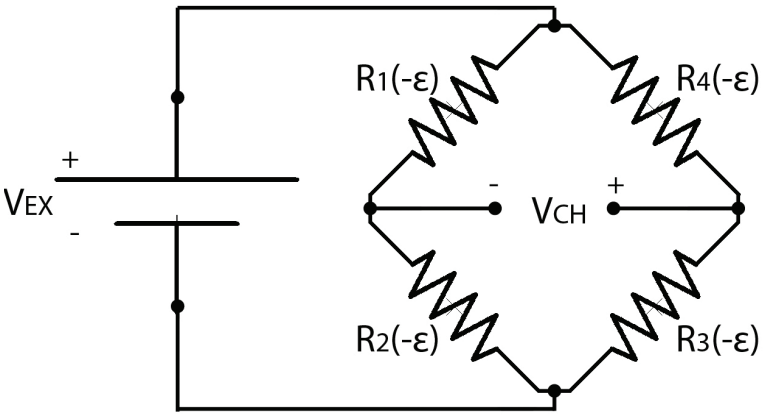


**Figure 20:** Full-bridge circuit topology showing four sensing elements, where $V_{EX}$ is the driving voltage and $V_{CH}$ is the measured output voltage. The full bridge circuit used four sensing elements to negate the effects of temperature variation amongst any of individual elements.

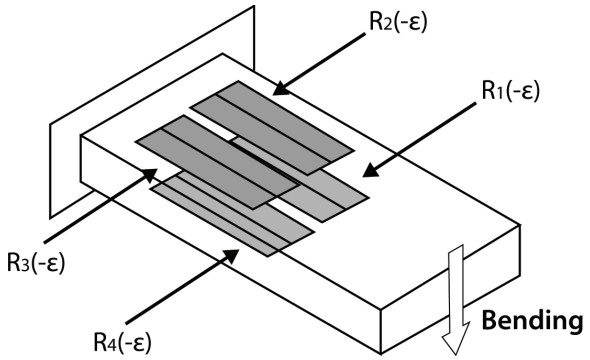


**Figure 21:** Full-bridge circuit strain gages mounted on a beam fixed at one end. This diagram shows the orientation of the gages required to measure bending strain and neglect shearing strain.

four resistive elements can be a sensing element, and this thesis focuses specifically on the full-bridge topology, which has four sensing elements.

The full-bridge circuit is highly sensitive to bending strain, and it does not consider axial strain, or shearing (Fig. 21) [31]. It has optimal use for biomedical applications because it is also temperature-compensating. Since strain gage operation is temperature-dependent, a single-bridge circuit must compensate for the change in resistance if the temperature of the mounting structure changes. Since all four resistive elements are strain gages in the full-bridge topology, the temperature change equally affects all resistors, effectively accounting for the changing temperature at all times (Fig.20) [31].

## *2.4 Skin Temperature*

The temperature of skin varies with changing environments, internal vascular circulation, and any irregularities in the local area. Skin temperature rests on average between 33°C and 36°C, but close proximity changes have a large effect on its full-range scale [26]. Direct contact with a material of a different temperature, or rapid changes in vascular temperatures, can both alter the measured skin temperature. This thesis considers the latter example for further investigation.

The venous infusion of TPN or vesicants can cause significant skin temperature

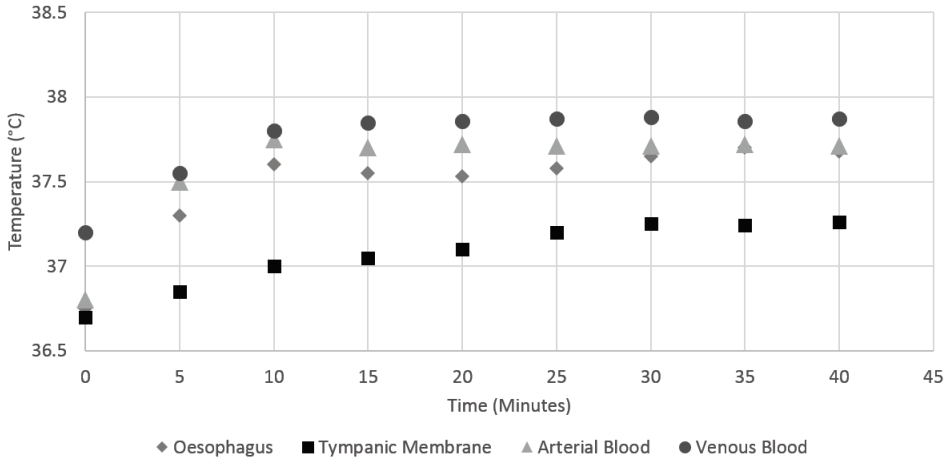


**Figure 22:** Graph showing various internal body temperatures. Venous blood temperature measured at the Jugular Vein is around 37.75±0.13°C, and is the highest of all other internal temperatures measured. This temperature radiates to the surface skin. If any liquids stored at a different temperature are infused with the venous system, the change in temperature will also radiate to the surface skin. Hence, the change in temperature can be detected with skin surface temperature monitoring.

changes since the temperature of these solutions vary from the internal temperature of the vascular system. The venous vascular system rests at a temperature around 37.75°C (Fig. 22) [34]. TPN is kept refrigerated at around 4°C but is brought to room temperature before infusion, approximately 24°C [14]. When a patient undergoes IV therapy, the TPN infusion and venous temperature difference is approximately 10°C.

Humans and most mammals are homeothermic, meaning that they maintain a very narrow body temperature by using regulation mechanism when changes are detected [51]. To maintain a stable body temperature, the body must regulate itself to allow for heat production when heat is lost. The body uses the external environment to balance the temperature through thermal exchange at the skin-air interface. This exchange can occur by radiation, conduction, convection, or evaporation and can result in perspiration or skin-drying as a result. Conduction, the process used to transfer the change in heat from the venous system to the skin, occurs by thermal energy collisions between adjacent molecules. The thermal exchange occurs by direct contact between both surfaces at different temperatures. Radiation, the process

used in passive thermal exchange, is a process by which heat is exchanged with the environment via electromagnetic waves. The rate of exchange is determined by the temperature differential at the skin-air interface [51]. In the case of TPN infusion, the body transfers the resulting 10°C reduction in temperature to the skin via conduction. Once the reduction is transferred to the skin-air interface, the temperature drop can be recorded externally, after which radiation will attempt to restore the skin and venous system temperatures.

Measuring skin temperature has been done optically using imaging or laser techniques, but a common and cost-effective way to measure and record skin temperature is to use resistance temperature detectors (RTD). RTD's have the unique ability to linearly change their total resistance with a change in temperature. By using Ohm's law (Eq. 1), a change in resistance can be sensed by driving the element with a constant current source and monitoring the voltage change across it. The linearity coefficient and full-scale range of the element is based on the material used to fabricate the RTD. Platinum, nickel, and copper are all commonly used for RTD fabrication due to their material behavior over a large range of temperatures, but platinum provides the larger full-scale linear resistance versus temperature behavior, from -272.5°C to 961.78°C [32].

The linear relationship between resistance and voltage that make RTD temperature sensing possible is defined by the Callendar-Van Dusen Equation. Both Hugh Longbourne Callendar and M.S. Van Dusen contributed to the linear observation in the early 20th century, with Van Dusen simplifying the findings by Callendar. Callendar found that the temperature of a platinum RTD could be measured by knowing its resistance, its fundamental value $\alpha$ determined from the boiling point of water, and the boiling point of sulfur $\delta$ (Eqn. 13) [16]. Van Dusen went on to discover a quadratic relationship between temperature and resistance based on empirical results found using the freezing point of mercury (A), the normal sublimation point of carbon

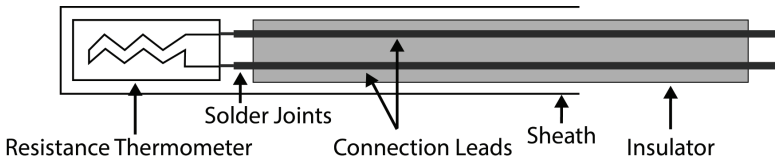


**Figure 23:** Diagram showing physical construction of thin-film RTD element. The element is enclosed in a silicone elastomer cover for protection from liquids. The typical resistance used for RTD's is 100Ω.

dioxide (B), and the normal boiling point of oxygen (C) (Eqn. 14). For a platinum RTD with R(0) = 100Ω, the constants are empirically found to be: $\alpha = 0.00385$, $\delta = 1.4999$, A = 3.9083 x $10^{-}3$, B = -5.775 x $10^{-}7$, C = -4.183 x $10^{-}12$ [21].

$$t = \frac{1}{\alpha}(\frac{R}{R_0} - 1) + \delta(\frac{t}{100} - 1) * \frac{t}{100} \tag{13}$$

$$R(t) = R(0)[1 + A * t + B * t^2 + C * t^4] \tag{14}$$

RTD's are manufactured as thin-film elements, with a 10nm thick metal wire wound in a zig-zag pattern and bonded to a plastic substrate. The RTD metal wire ends are terminated with flat metal pads for connection to longer lead wires. Additionally, the element is often coated in plastic or silicone material for protection against element fatigue or liquid contact (Fig. 23) [32].

For a typical platinum-based RTD, its resistance varies ±50Ω over a temperature range of 250°C. However, analog circuitry must be designed to take advantage of the elements 0.1°C resolution and to be read digitally. The RTD can be driven in a three-wire configuration or four-wire configuration, which helps minimize the effects of the lead wire's added resistance. To drive the circuit, a 2mA howland-pump current source can excite a 100Ω RTD enough to output a ground-referenced voltage of about 200mV. By using an instrumentation amplifier to gain the RTD output, the circuit can be designed to amplify only the change in temperature and cancel out the bias voltage that the RTD rests at for a given calibration temperature. In the case of using an RTD for skin temperature measurements, choosing the calibration temperature as

the average skin temperature can help utilize the RTD's accuracy and resolution for a smaller scale of interest just around this value. Also, by choosing the instrumentation amplifier's reference voltage as $Vcc/2$, the circuit can utilize the amplifier's full rail-to rail operation for the differential measurement. Finally, a filtering stage must be used to limit the noise interference from high frequency oscillation and 60Hz power line noise.

# CHAPTER III

# INSTRUMENTATION DESIGN

The automated non-invasive detection of IV infiltration can potentially alleviate the burden of monitoring multiple patients placed on nurses, greatly improve the quality of care offered by NICU's, and ultimately reduce the number of cases in which infiltration results in irreversible effects. Though there have been previous attempts to detect infiltration, they have all fallen short in presenting a solution that can be appropriate for use amongst neonates in a hospital setting. This chapter will cover the method by which automated non-invasive detection can be achieved and realized in a low-cost and low-power device. The following sections will present the proposed infiltration sensing technique, mechanical design, electrical design, and finally a review of the system level design.

## *3.1 Sensing Technique*

The proposed sensing technique is designed on the basis of monitoring three responses to an infiltration: the rapid cooling of skin, the reduction in bioimpedance, and the stretching of skin all proximal to the infiltration site. This technique focuses its efforts on only using non-invasive sensing as a method to detect an infiltration, and this becomes very important to the proposition when considering the goals of this design and the failures of others. While invasive monitoring of venous activity or even integrating infiltration sensing directly into the catheter have been proposed, these methods have a large associated risks that can offset their value criterion. When 1 in 25 hospital patients on a given day are found to have contracted a hospital-associated complication in the United States alone, solving the problem at hand non-invasively gives the proposed design the upper hand when it comes to feasibility and overall

**Table 5:** ADC Sampling Rates for Sensing Modalities Based on 1MHz Clock - based on data provided by [47]

| **Modality** | **Sampling Rates Possible** | **Modulator Frequency** | **Sampling Rate Chosen** |
|---|---|---|---|
| Bioimpedance | 8-860 SPS | 250 kHz | 64 SPS |
| Strain | 8-860 SPS | 250 kHz | 64 SPS |
| Temperature | 600-38000 SPS | 7.8-500 kHz | 9600 SPS |

cost associated [27]. In fact, the scientific basis of the non-invasive sensing methods used can prove to be even more reliable than the non-invasive methods previously proposed when detecting infiltration amongst neonates.

The choice of these three sensing modalities was based on the symptoms associated with an infiltration and the system requirements of sensing them. The detection speed of the system is vital to building a device that can help alert a nurse of an infiltration before the solution has leaked into the nearby tissue. It is also important that the system not alert medical staff if some of the symptoms are detected but an infiltration has not occurred, resulting in false positives. Since the symptoms being monitored are not completely independent of each other, the system can actually predict the outcome of other responses after extensive characterization. The redundancy built into monitoring all three can then maintain a fast response time system-wide while also attempting to reduce false positives. Together, the sensing elements can record up to 64 samples per second, allowing for an extremely time-accurate response to an infiltration. Table 5 shows the sampling rates available by all of the sensing modalities, and the rates chosen based on Nyquist requirements and for overall performance. Even by incorporating redundancy in the sensing technique, the proposed system could potentially be able to capture an infiltration within seconds while still being lightweight and affordable enough to be used in NICU's worldwide.

## *3.2 Bioimpedance Characterization*

Measuring skin and tissue bioimpedance as introduced in Chapter 2.2 requires high dynamic range analog circuitry. The basics of measuring bioimpedance rest on Ohm's Law (Eq. 1). Bioimpedance can be measured using a clean, low-amperage AC current supply source to excite the site of interest and measuring the differential voltage. This voltage difference will likely be too small to be detected with respect to the noise floor of processing devices ($\sim$370$\mu$V), so it must be gained and filtered before converting the difference into impedance using digital signal processing.

The mechanical placement of the electrodes used for bioimpedance sensing was chosen specifically with the IV catheter site and technology in mind. As mentioned in Chapter 2.1, the superficial dorsal vein is a common venipuncture site amongst infants, hence this site is where measuring changes in bioimpedance will be critical. This site is located at the distal radio-ulnar joint, near the wrist. The system will also use tetrapolar measurements for measuring impedance, which requires four seperate electrodes, a pair for current excitation and another for voltage sensing. Since we want the current to excite the tissue at the catheter site, the electrodes must be

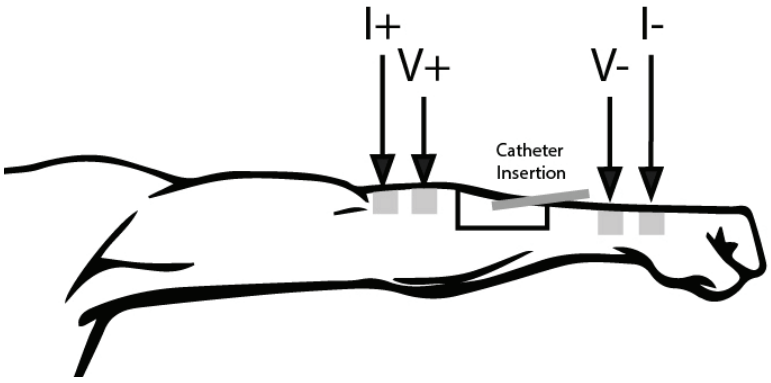


**Figure 24:** View of arm showing catheter insertion site and tetrapolar bioimpedance measurement electrode placement. Since our interest is in measuring liquid content around the catheter site, the electrode pairs must be placed around this site but in accordance with the tetrapolar measuring technique. This means current must be injected using the external pair of electrodes, and voltage must be sensed using the inner pair of electrodes.

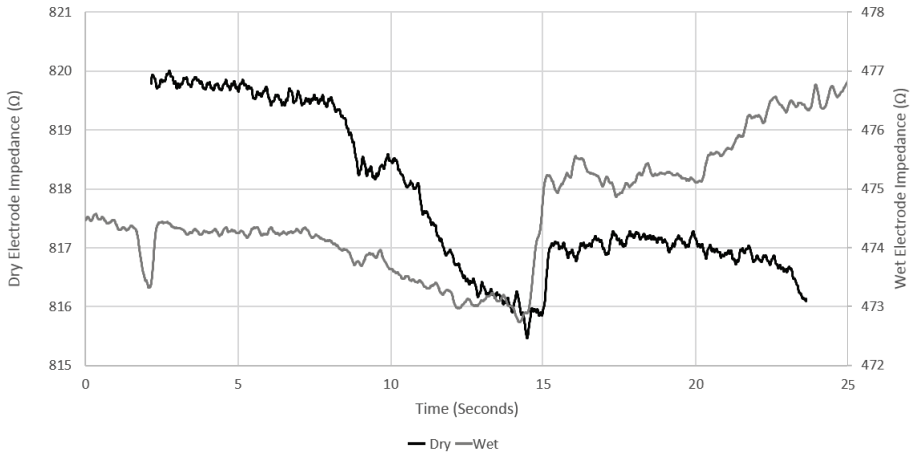


**Figure 25:** Graph showing measured impedance comparing dry (Copper Tape) and wet (Ag/AgCl) electrodes. The measurement set up is shown in Figure 26. Both electrode types have very similar performance, but the dry electrodes measurement reads approximately 340Ω above the wet electrodes. This can be due to a multitude of reasons, some of which include electrode placement, fixation, and adhesive contact. However, both electrodes were able to measure the change in bioimpedance equally, as can be seen at t=7s. The change in bioimpedance was induced by injecting conductive liquid into the meat, and will be further described in Chapter 4.

placed around the site axially. Figure 24 shows the placement chosen for this site.

The dry electrodes used for measuring bioimpedance are made of copper tape, which is a conductive material that has proven to give similar performance to wet silver-chloride(Ag/AgCl) electrodes (Fig. 25). This allows the electrodes to be worn comfortably on the skin, without the use of any adhesive. It also means that the same electrodes become reusable and extremely cost efficient, with copper tape costing just a fraction of an Ag/AgCl electrode.

It is also important to consider the resistance of the electrodes themselves. The real impedance of a wet Ag/AgCl electrode is approximately 20Ω. For copper tape with resistivity $\rho = 1.68 * 10^{-8}$, Width = 20mm (millimeter), thickness = 0.05mm, and Length = 200mm, the real impedance of the copper tape is approximately 330mΩ (Eq. 15).

$$R = \rho * \frac{L}{Wt} \tag{15}$$

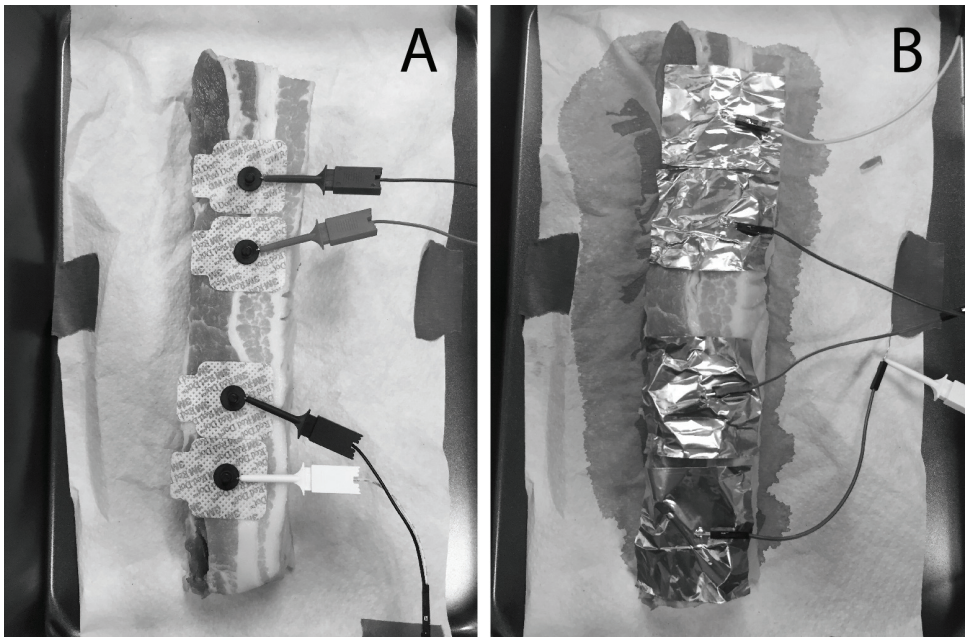


**Figure 26:** Measurement setup for comparing bioimpedance measurement from 3M Ag/AgCl Wet Electrodes vs. Copper Foil Dry Electrodes. A cut of pork belly was used for taking the measurement, with its dimensions outlined in Figure 48.

To ensure proper operation of the dry electrodes, there must be tight skin contact between the copper and the skin surface. This can be accomplished by using velcro or a neoprene sleeve to secure the position of the electrodes. Figure 27 shows the four dry electrodes taped to a neoprene backing for use as cuffs around the catheter cite. The cuffs also have velcro straps for adjusting the radius of the cuff to form a tight fit around the patient's wrist and arm.

Texas Instruments's Analog Front-End 4300 (AFE4300) incorporates all of the analog and digital circuitry required to measure bioimpedance, and it will be the basis of the electronics discussion. The AFE4300 is an application-specific integrated circuit (ASIC) designed by Texas Instruments specifically for measuring bioimpedance for medical applications with low-power requirements. It draws 970$\mu$A during bioimpedance measurements, and 100$\mu$A during sleep-mode. Table 6 shows the relevant electrical characteristics for the AFE4300 bioimpedance measurement.

**Figure 27:** Adjustable cuffs made for tetrapolar bioimpedance measurement that use copper tape as the dry electrodes. The outer electrodes are for current injection, and the inner pair for voltage sensing.

**Table 6:** Electrical Specifications for the AFE4300 Bioimpedance Measurement - based on data provided by [47]

| **Parameter** | **Typical** | **Unit** |
|---|---|---|
| Excitation Source | 375±20% | $\mu A_{RMS}$ |
| Dynamic Range | 0-2.8 | kΩ |
| Measurement RMS Noise | 0.1 | Ω |
| DAC Resolution | 6 | bits |
| DAC Full-Scale Voltage | 1 | $V_{pp}$ |
| DAC Sample Rate | 1 | MSPS |
| Input Impedance | 50 | kΩ |
| Gain | 0.72 | V/kΩ |
| Common-Mode Rejection Ration | 75 | dB |
| Nonlinearity | 0.15 | % of FS |

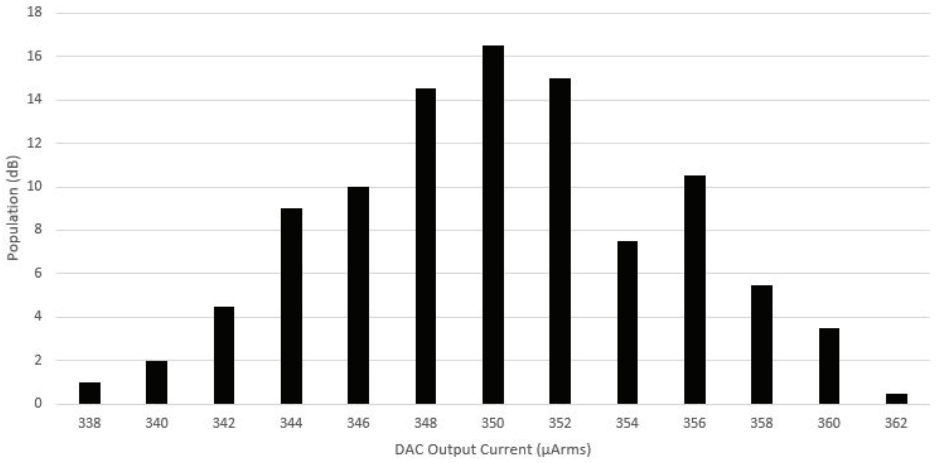


**Figure 28:** Variation of output current based off 300 devices measured, with mean output current of $350\mu A_{rms}$. This is a safe amount of current to inject into the body without any harm, and also enough to drive the measured site enough to respond with a measurable voltage. Data provided by TI [47, 50].

The AFE4300 output current is approximately $350\mu A_{rms}$, with its measured distribution following a Gaussian shape (Fig. 28). This is generated via a direct digital synthesizer, using the input 1MHz clock and a digital-analog converter (DAC). The frequency of the AC current can be digitally programmed by modifying the DAC, and it is set to 64kHz for this system. After a filter stage used to reject any noise artifacts, the current is injected into the body. An oscilloscope screen capture of the input current is shown in Figure 29.

The analog circuitry in the AFE4300 is designed to handle a load between 0-2.5kΩ, which is well beyond the range of interest for this system. The AFE4300 has a linear relationship between output voltage and measured impedance as shown in Figure 30. To confirm these results, it was necessary to test multiple loads, known as phantom loads, around the range of interest. After affirming the linear relationship between voltage and bioimpedance, it was also necessary to see the distribution of measured impedance for a fixed load to understand the possible noise artifacts during measurement. Figures 31 and 32 show the results from these tests.

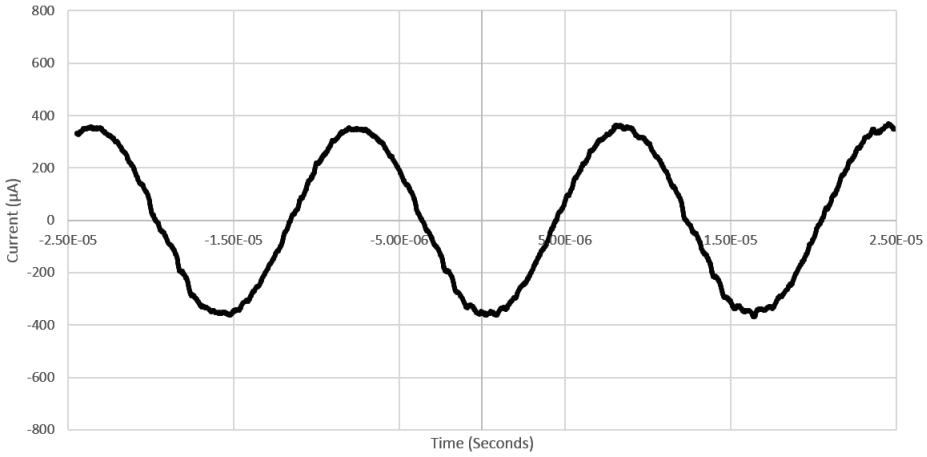


**Figure 29:** Oscilloscope capture of Bioimpedance excitation current source output from AFE4300 in Four Wire Resistance mode. Measurement was taken over a 980Ω load resistance. Data was processed in MATLAB using a moving average filter using the vector $y(n) = \frac{1}{20}x(n) + \frac{1}{20}x(n+1) + ... + \frac{1}{20}x(n+19)$.

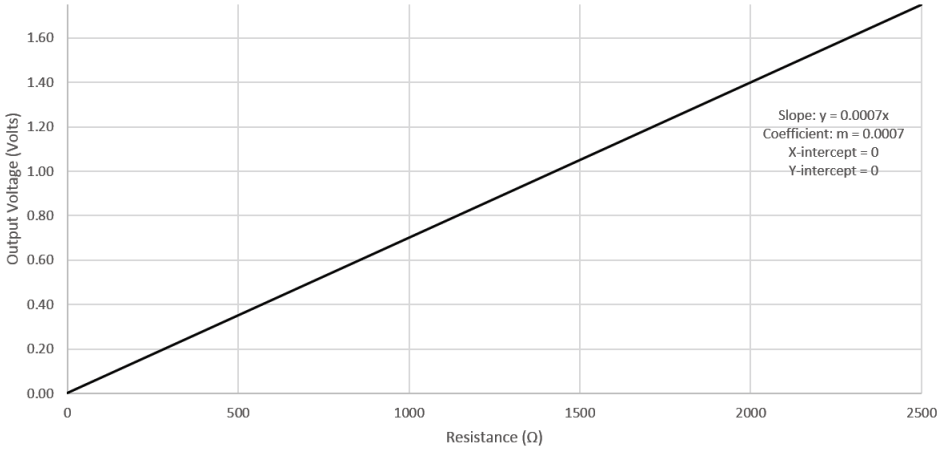


**Figure 30:** Graph showing linearity between output voltage and measured resistance for AFE4300 using Full-Wave Rectifier mode specified by the datatsheet. This output voltage is gained by differential amplifier by the AFE4300, then the gained output is and converted back to measured impedance using Ohm's Law. Correlation slope, coefficient, and intercepts annotated on graph. Data provided by TI [47].

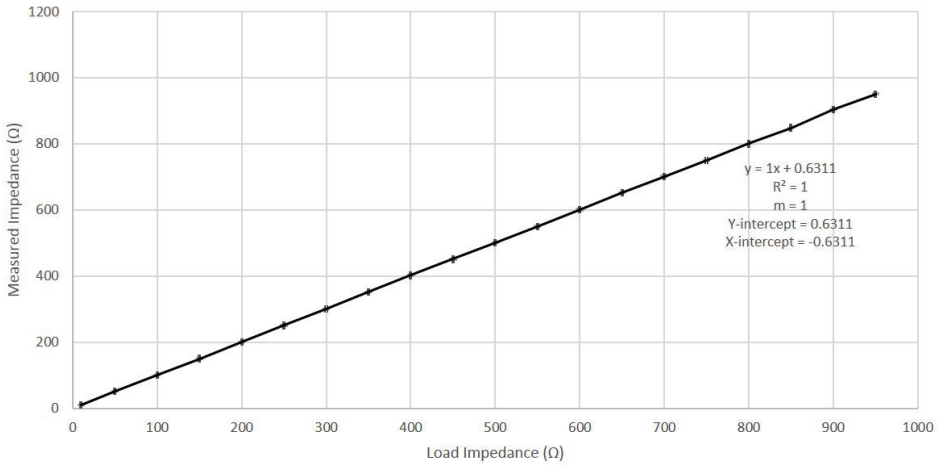


**Figure 31:** Impedance calibration by AFE4300 for various phantom loads in range of interest. Phantom load of every 50Ω between 10-960Ω were measured with the Bioimpedance front end circuitry. The output tracks the phantom loads with a linear coefficient of 1. This data is averaged over five data sets (N=5), and the standard deviation for each measurement was less than 3Ω, shown on the graph.

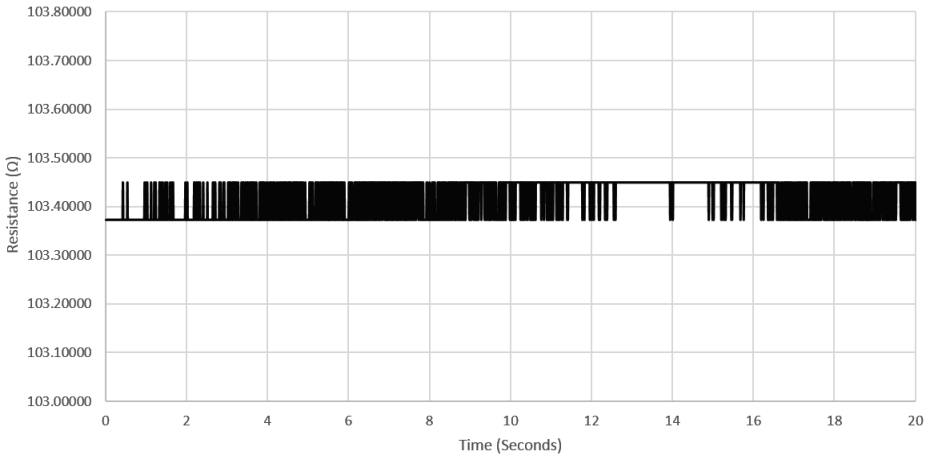


**Figure 32:** Graph showing drifting noise for a fixed impedance over a given time sweep. Measurement taken over 100Ω load, with noise variation resulting in ±0.05Ω. This is two orders of magnitude below the impedance changes of interest during IV infiltration.

## *3.3 Strain Characterization*

Measuring strain and deformation can be done by using strain gages, which are elements that have a linear relationship between resistance and strain applied. Chapter 2.3 briefly mentions the need for a Wheatstone bridge circuit to drive the strain gage, being that it allows for precise impedance calculation of the variable resistor. The small change in voltage across the bridge is amplified and filtered to determine the amount of strain applied. For this system, the strain gage is measured by the percentage change in voltage from an inflection or deflection of the gage with respect to its resting voltage.

For this system, a full-bridge topology will be used for the benefit of its temperature compensation effect. The full bridge topology uses four strain gages that can all be actively sensed, which allows the system to use a single full-bridge input to capture strain measurements radially at the IV catheter site. The strain gages must be placed equidistant from one another and orthogonal to the length of the arm to measure skin ballooning or edema formation anywhere around the site. It is also important to place the strain gages all with the same Z-orientation, such that the pattern is facing outwards and the backing material is in contact with the skin. This will ensure that all changes in strain are calculated for with the correct sign convention. These gages are to be mounted on a neoprene sleeve around catheter site, with enough compression to make the gages skin-tight. Figure 33 shows a cross section view of how the strain gages will be placed around the IV site.

The strain gage selected for this system is the Omega SGD-6/120-LY41 [35]. It is a single axis strain gage with constantan foil pattern. It is specified to be mechanically strong, with a small bending radius and a broad temperature range. Each gage has a nominal resistance of 120$\Omega$, while its maximum inflection/deflection resulted in a $\pm 1\Omega$ change. Below are figures showing the strain gage's physical dimensions (Fig. 34) and its measured impedance response to changing the inflection/deflection angle

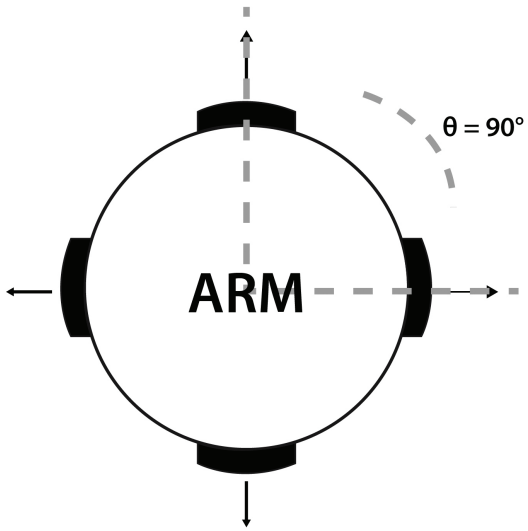


**Figure 33:** Cross-section of radio-ulnar joint showing full-bridge strain gage placement for capturing skin ballooning. Each strain gage (black) must be facing the same upwards direction for full bridge operation, and they must all be placed with their gage patterns orthogonal to the length of the arm to capture strain.

(Fig. 35). The strain gage was inflected and deflected along a protractor, and its resistance was measured with a digital multimeter with milliohm resolution (Fig 36).

The full-bridge circuit is interfaced with the Texas Instruments Analog Front-Eng 4300 (AFE4300), aforementioned in Chapter 3.2. The voltage source that supplies the Wheatstone bridge is generated by a low-dropout voltage regulator (LDO) on-board the AFE4300. The bridge voltage, in the range of ±5mV, is amplified by operational amplifiers (Op Amp) in an instrumentation amplifier topology. A gain setting resistor

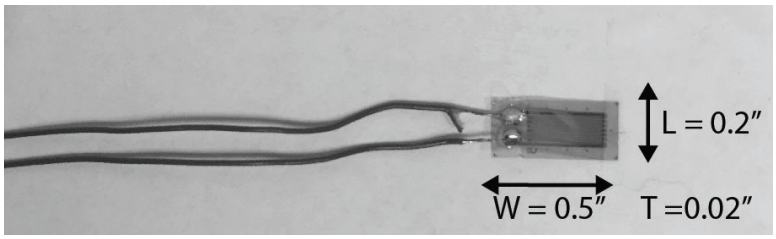


**Figure 34:** Image of Omega SGD-6/120-LY41 strain gage with physical dimensions annotated. Electrical leads with silicone sheathing attached for interacing to driver voltage and rest of bridge circuit. Solder joints attach these leads to pads exposed on the gage pattern. These leads can add significant resistance when measured in series with the gage pattern, hence all leads for the strain gages used should be trimmed to the same length for optimal bridge performance.

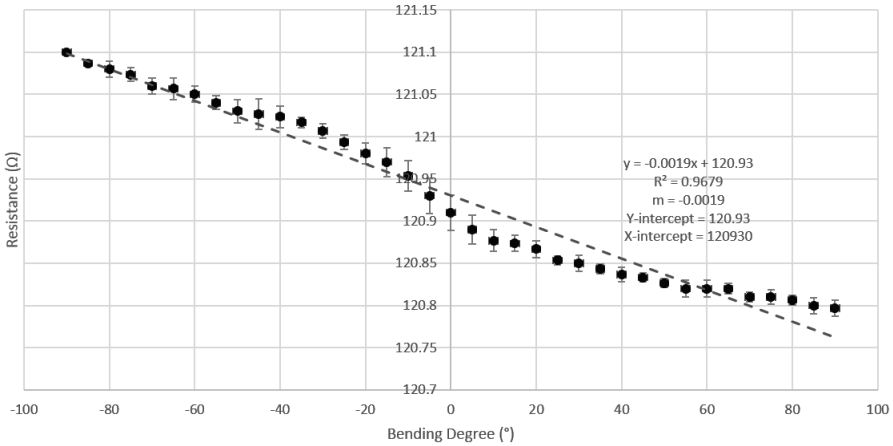


**Figure 35:** Measurement of individual strain gage's impedance response by inflecting and deflecting the gage $\pm 90°$. The maximum and minimum detectable strain angles based on measured impedance are $90°$ and $-90°$ respectively. The resolution of the strain gage was measured to be $16\frac{m\Omega}{°}$. This test was conducted by inflecting and deflecting an Omega strain gage from -90°-+90° along a protractor and measuring the voltage output from a precision multimeter. A linear trend line with coefficient, intercepts, and $R^2$ are shown on the plot. Data is plotted as average of three datasets (N=3) with standard deviation shown on the graph.

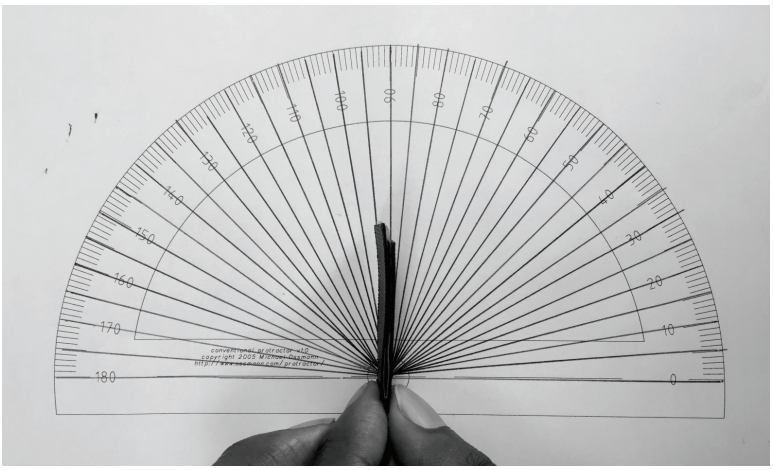

**Figure 36:** Image of Omega SGD-6/120-LY41 strain gage placed in silicone covering used for precise inflection and deflection measurements along a protractor with degrees marks every 5°.

**Table 7:** Electrical Specifications for the AFE4300 Strain Measurement - based on data provided by [47]

| Parameter | Typical | Unit |
|---|---|---|
| Input-Referred Noise | 68 | n$V_{RMS}$ |
| Bridge Supply Voltage | 1.7 | V |
| Output Current | 20 | mA |
| Enable/Disable Time | 1 | mS |
| Offset Error | 80 | $\mu$V |
| Common-Mode Rejection Ratio | 95 | dB |
| Gain Nonlinearity | 0.01 | % of FS |

($R_G$) external to the ASIC is used to set the gain of the first stage of amplification, and the gain of second amplifier stage can be selected by programming the feedback resistor value ($R_{FB2}$) using a microcontroller (Eq. 16).

$$A_{total} = A_1 * A_2 = \left(1 + 2 * \frac{100k}{R_G}\right)\left(\frac{R_{FB2}}{80k}\right) \tag{16}$$

Selecting different gain resistors greatly affects the full-scale range for the output swing of the circuit, and testing multiple resistor's output voltage range resulted in setting $R_G = 200\Omega$, $R_{FB2} = 80k\Omega$, and ultimately $A_{total} = 308$ (Fig. 37). With the voltage across the bridge being approximately 3±1mV during an inflection/deflection, these gain settings offered an output voltage of 0.85V and a swing of ±0.3V. This is well within the electrical specifications provided by the AFE4300, shown in Table 7. Since the ADC has a 16 bit resolution $\left(\frac{+FS}{2^{15}}\frac{V}{LSB}\right)$, this results in the system being able to sense changes in strain with a resolution of $9\mu V/LSB$. This output voltage will be measured as percent change from the resting voltage of the strain gage for future DSP analysis. In terms of percentage change, the resolution of the strain gage system is 0.009%.

The change in strain is visualized by a percent change from the resting voltage. While it is not yet known the medical thresholds for how much the skin balloons when an infiltration occurs, a percent change measured radially to the infiltration site can

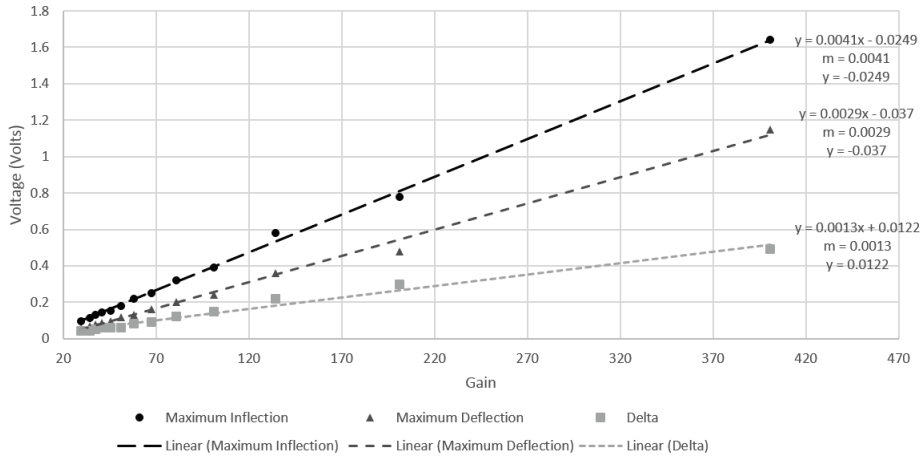


**Figure 37:** Measurement of Full Scale Range vs. Gain for AFE4300 strain mode instrumentation amplifier stage. Results obtained by applying maximum inflection/deflection angle to Omega strain gage ($Z_0 = 120\Omega$) and measuring difference between maximum and minimum voltage. The setting with the largest full-scale range provides the highest resolution for ADC conversions. Trendlines show linear relationship between gain and voltage output, with linearity coefficient and y-intercepts annotated on graph.

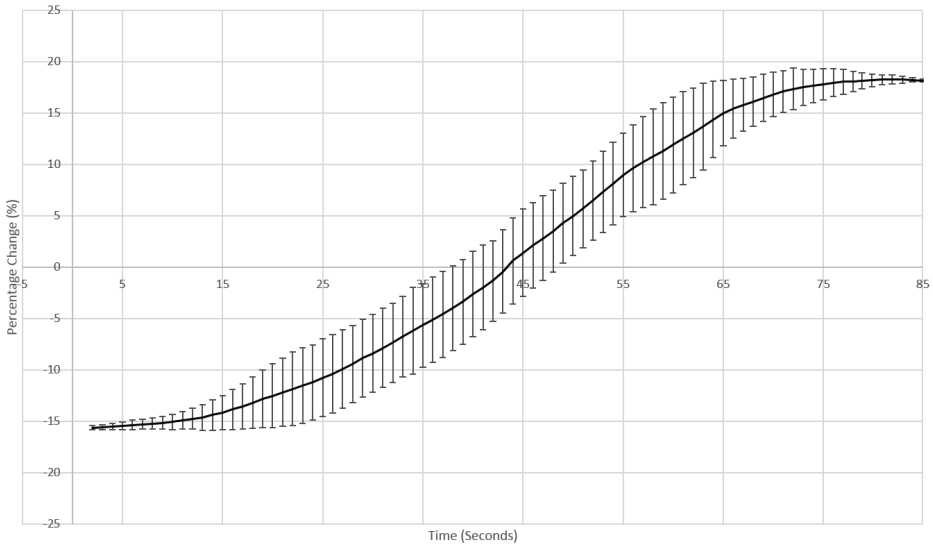


**Figure 38:** Measurement of AFE4300 strain output plotted as Percentage Change vs. Time for an maximum inflection and deflection using Omega strain gages in a full-bridge topology. Data plotted as average of eight sets (N=8), with error bars showing standard deviation of maximum ±4% towards the middle of the plot. This can be attributed to slight timing mismatch between successive strain measurements.

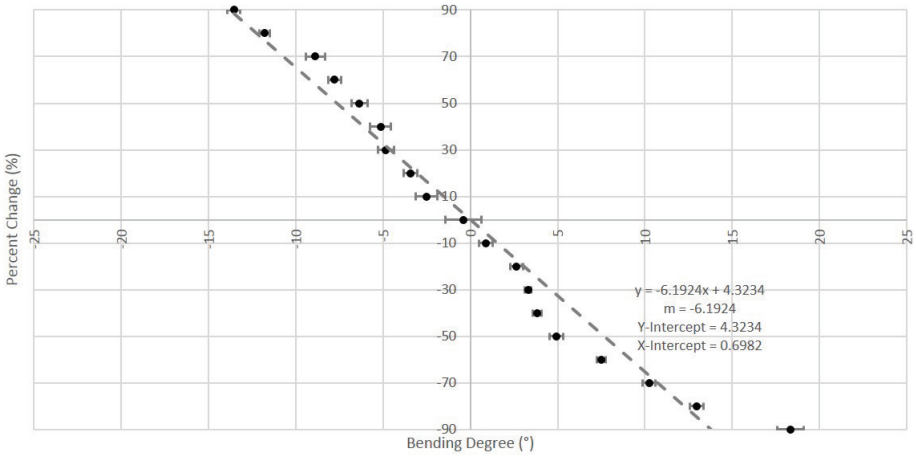


**Figure 39:** Measurement of AFE4300 strain output plotted as Percentage Change vs. Bending Degree for any bending degree applied to the gage orthogonal to its pattern. This test was conducted by inflecting and deflecting an Omega strain gage from -90°-+90° along a protractor and measuring the voltage output from the AFE4300. The output follows a linear trend, of which the slope and intercepts are annotated on the graph. This data is averaged over five data sets (N=5), and the standard deviation for each measurement was less than 1%, shown on the graph.

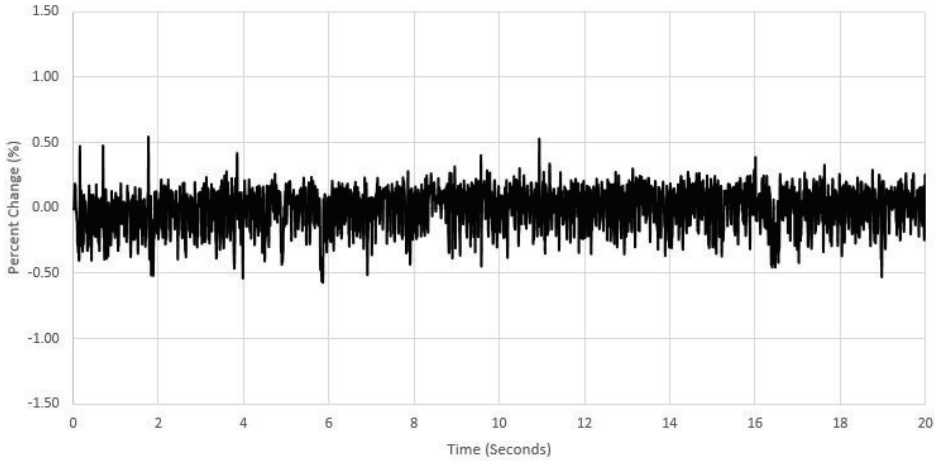


**Figure 40:** Measurement of the variation in strain output for the strain gages at rest, with the maximum variation being ±0.5%. This variation is tolerable for our application since we are looking to identify percent changes of a much higher magnitude (±15%). Acquired using AFE4300, plotted as Percentage Change vs. Time using Omega strain gages in a full-bridge topology.

provide information with regards to whether any of the four gage locations are experiencing unexpected changes in strain. Combined with the other sensing modalities, this modality can be used with respect to the original skin strain measurement as a confirmation of how large the edema has become since the infiltration was first detected. Figure 38 shows a typical output from a maximum inflection and deflection as a percentage change from the original strain applied, and Figure 39 shows the change in percentage degree-by-degree for $\pm 90°$. The data shown is averaged from 8 different bench-top trials, and the experimental setup can be seen in Figure 36. Figure 40 shows the variation in resting voltage over a given amount of time to help visualize the signal-to-noise ratio (SNR).

## *3.4 Temperature Characterization*

Measuring temperature reduces the time of detecting an infiltration, and in turn greatly improves the likelihood of medical staff being able to cure the region before the leaking solution travels far into the body. One of the first seen symptoms of an infiltration is the rapid decrease in temperature at the IV catheter site, hence it is extremely important to sense changes in skin temperature with a high resolution. As described in Chapter 2.4, RTD's can be employed as a low-power method to measure skin temperature, while also providing a high resolution. By exciting the RTD with a clean DC current source, the system can employ the RTD's linear relationship between temperature and voltage. The temperature range can be set by taking the difference between the voltage at the RTD and another generated calibration voltage using an instrumentation amplifier. Finally, by filtering the output for high frequency noise and 60Hz powerline noise, the analog voltage can be converted to a digital value using an ADC.

The selection of the right RTD for this application was made based of the need for a compact, high resolution sensor. The Measurement Specialties RTD327 operates

over a large temperature range with a relatively high resolution of ±0.1°C, and was small enough to fit on an infant's arm [29]. The RTD327 has a nominal resistance of 100Ω, and is made of a platinum element on a polyimide substrate. It also has a silicone casing for comfortable placement on the skin. Though the RTD is specified to have a temperature range between -50 to 155°, our application only requires a small range around the resting skin temperature. Figure 41 shows an up-close image of the RTD with its mechanical dimensions annotated.

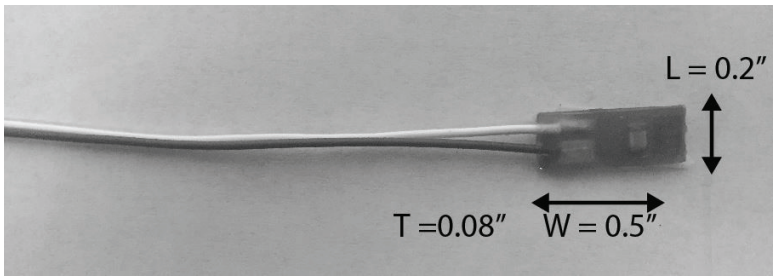


**Figure 41:** Diagram showing the mechanical dimensions of Measurement Specialties RTD327. The silicone elastomer cover is shown enclosing the element and solder joints, ensuring contact between the lead and pad even under duress.

This RTD was characterized against measurements taken from a digital thermometer (Fig 42). The noise floor of the RTD and analog circuitry gives the system the ability to detect temperature within the highest of resolution. Figure 43 shows the fluctuations in room temperature over a given time as measured by the RTD327 and custom analog circuitry.

To detect a change in temperature just at the IV site and not an overall body temperature change, two RTD's must be used and placed away from each other. By placing one near the elbow and another at the IV catheter site, a valid estimate of just the differential skin temperature can be made. These sensors can be mounted in the same neoprene cuffs used for the bioimpedance dry electrodes (Fig. 27). Figure 44 shows the placement of the RTD's on an infant arm for detecting a leakage.

The analog circuitry used to excite and gain the RTD output had to be custom designed to achieve high resolution over the full scale voltage range. A Howland

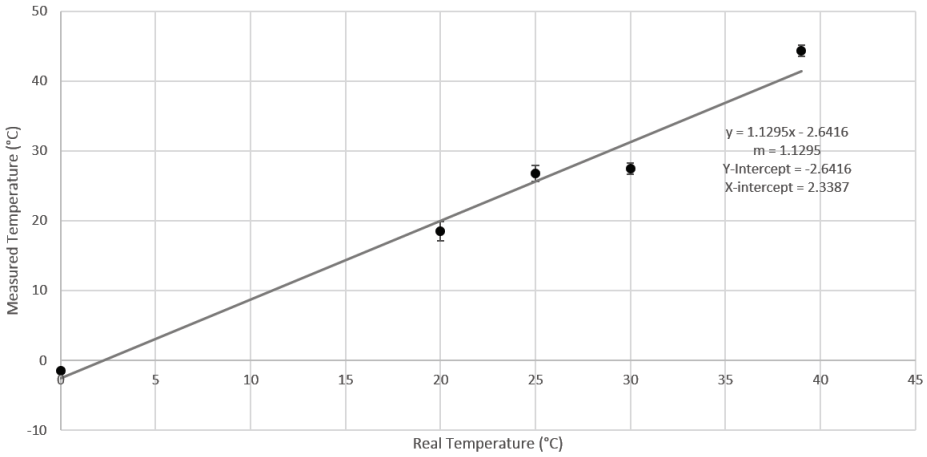


**Figure 42:** Graph showing linearity between measured and real temperature taken by calibrating the sensor at various temperature points, including ice, room temperature, hot liquids, and variants in between. Data averaged over (N=3) sample sets, with standard deviation maximum of $\pm 1.5°C$. Linear trendline plotted after visual inspection with coefficient and intercepts annotated on graph.

Pump was chosen to generate and regulate the current required to excite the RTD. A 2mA current source is recommended for a platinum based RTD, hence the resting differential voltage across the element is 200mV. The circuit diagram for the Howland Pump is shown in Figure 45.

The Op Amp chosen for the Howland Pump and the rest of the analog circuitry is the LMC6462, with a rail-to-rail input common mode range (ICMR) [46]. Having a large ICMR was essential since the input voltage to the first Op Amp stage would be in the range of millivolts (Fig. 46). The LMC6462 also has very low noise contribution and a relatively low offset voltage for the inputs the analog circuitry uses [46]. Thus, the input signals have minimal artifacts from the gain stage itself. Since the output is also rail to rail, the amplifiers can gain the analog signals high enough utilize the full range of the voltage rails onboard (3.3V and Ground). In turn, the ADC can be used to its full range possible and offer the highest resolution per LSB.

Once the RTD is excited by the 2mA current source, the analog signal output must be gained with respect to a reference voltage set externally. For this, an instrumentation amplifier will be used with an external voltage reference. Since the

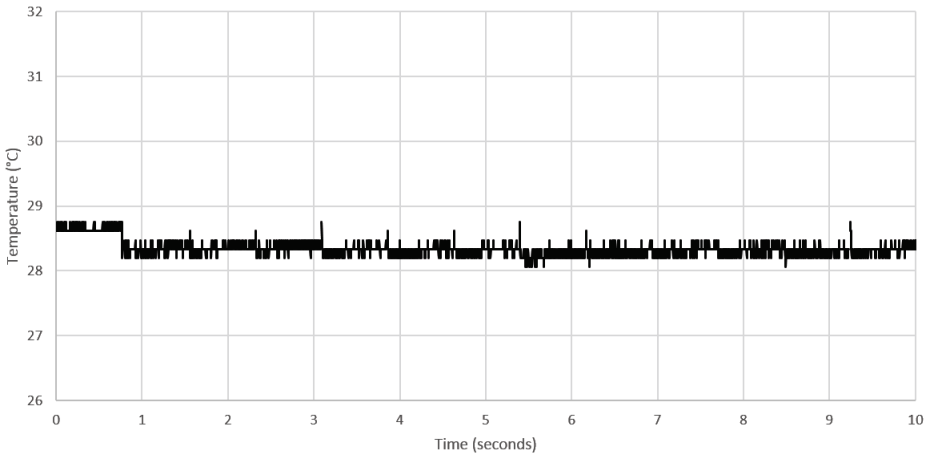


**Figure 43:** Distribution of room temperature RTD measurement, resting at 28.5 ±0.25°C. This measurement was taken using custom analog circuitry and the Measurement Specialties RTD327 at room temperature.

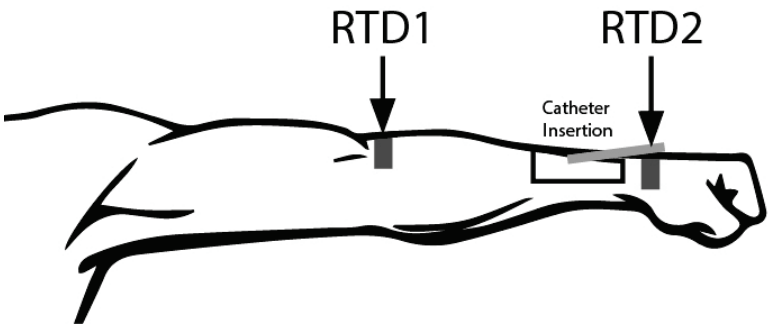


**Figure 44:** Diagram showing placement of both RTD's on an arm for detecting the rapid drop in temperature associated with an infiltration. RTD1 is for detecting constant skin temperature, and RTD2 is for detecting catheter site temperature. By monitoring the differential temperature across the site, an infiltration can be detected based off a sharp decrease.

temperatures of interest for the design are between $0°C$-$50°C$, the reference voltage for the instrumentation amplifier must be chosen such that the output voltage is $V_{mid} = \frac{V_{CC}-V_{SS}}{2}$ at 25°. In essence, the instrumentation amplifier is calibrated at the resting skin temperature, where anything above $V_{mid}$ means a temperature increase and anything below means a temperature decrease. $V_{mid}$ itself is generated by the REF1933 Voltage Reference IC [48]. By using the Callendar Van Dusen Equation (Eq. 13), the resistance of the RTD at $25°C$ is 109.7Ω. If driven by 2mA current source, the required voltage to calibrate the instrumentation amplifier for $25°C$ is

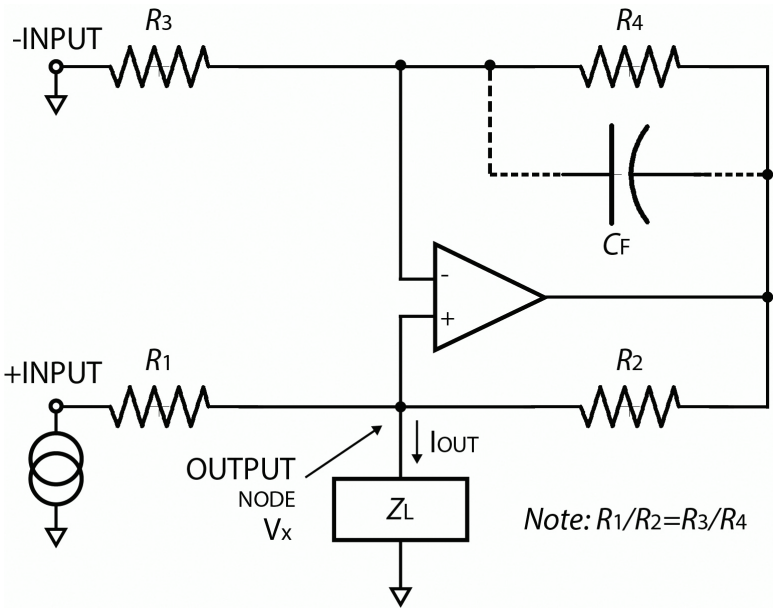


**Figure 45:** Circuit diagram of Howland Pump with passive components selected to deliver 2mA to the load. This is enough to drive the 100Ω for temperature readings, but a gain stage is required after driving the RTD to enable full-scale ADC conversions.

0.22V. Hence, a voltage divider is used to generate this voltage from $V_{mid}$.

The instrumentation amplifier used is the INA118, which is a low-power general purpose instrumentation amplifier for RTD sensor applications [45]. It also has a very low noise ($0.28\mu V_{pp}$) and offset voltage ($0.5\mu V$) performance, minimally affecting the RTD analog signal. The gain of the INA118 was set based off the temperature range of interest. When the RTD reaches the maximum temperature of $50°C$ and minimum temperature of $0°C$, the resistances are 119Ω and 100Ω respectively. With a 2mA excitation current, this translates to 0.238V and 0.2V respectively. Due to the INA118's ICMR being 1V above Ground and below VCC , these voltages need to be gained using a second stage of amplification. By using the LMC6464 with a gain setting of G=5, the output voltages at the maxima and minima are 1.19V and 1V. Since the negative terminal of the instrumentation amplifier is fixed at 0.22V gained by G = 5 to 1.1V, the maximum differential voltage in both the $50°C$ and $0°C$ cases is ±100mV. The instrumentation amplifier's gain can be set by an external resistor (Eq. 17), which is set to $R_G = 10k\Omega$ for G = 6. The voltage output rests at 1.65V at

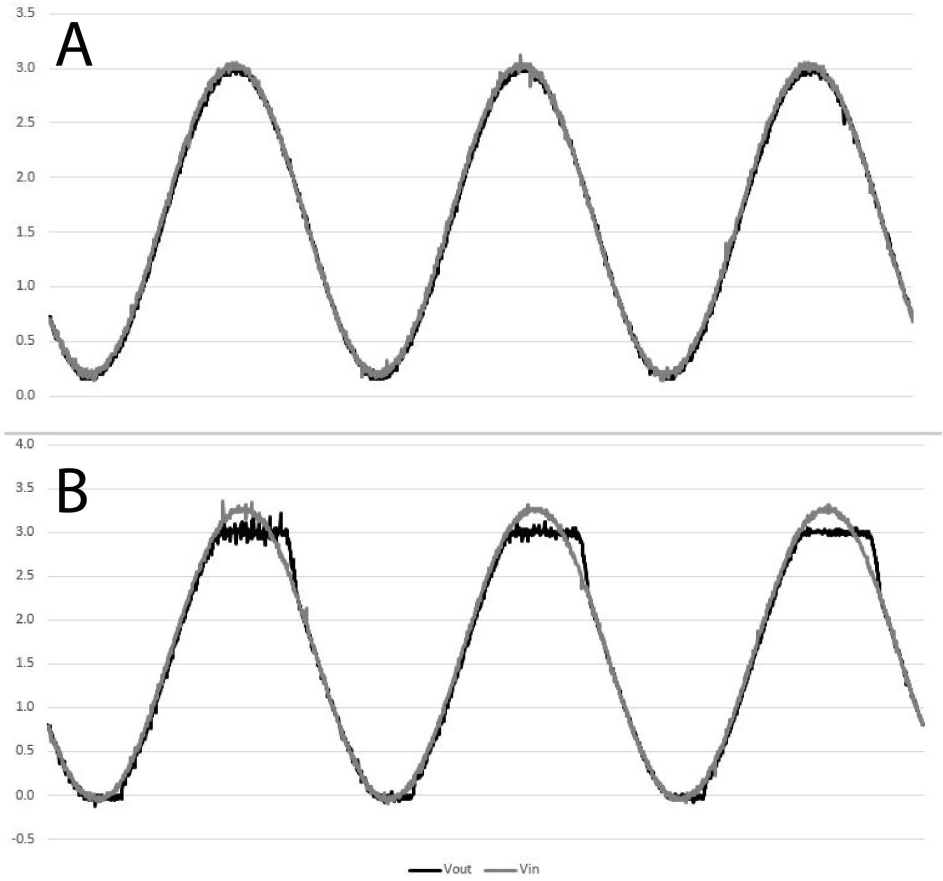


**Figure 46:** Testing LMC6462's Input Common Mode Range from Rail-to-Rail, where the A) Input voltage equals the IC power supply voltage B) Input voltage exceeds the IC power supply and clips at the rails.

$25°C$, and can swing between Ground and 3.3V for the temperature range $0°C$-$50°C$.

$$G = 1 + \frac{50k\Omega}{R_G} \tag{17}$$

The last stage before the ADC is the Sallen-Key Low Pass Filter. Made using the LMC6462, this stage filters out almost all AC frequency content from the signal, with its cutoff frequency set at 1Hz. Since the RTD signal is almost purely DC, the low pass filter used is able to attenuate all higher frequency resonance that can be generated by other analog IC's or by external power supply noise. The filter response is shown in Figure 47.

This RTD circuitry was designed to utilize the high resolution of the platinum RTD

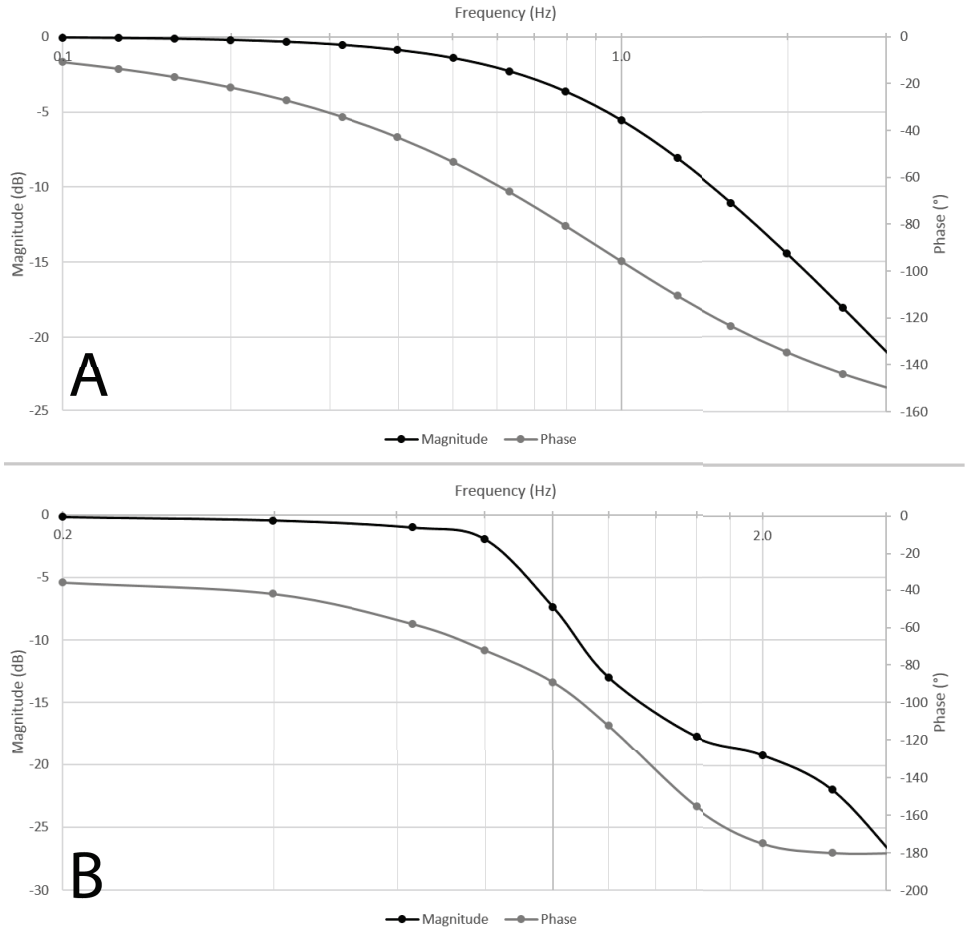


**Figure 47:** Bode response of Sallen-Key Low Pass Filter using LMC6462, with: A) Simulation measurements obtained using LTSpice IV and B) Measured performance by using gain values and time delay of output vs. input signal at frequency increments from oscilloscope measurement.

to be able to read the temperature range of interest across the full-scale range of the ADC. Another important consideration is the power consumption of the circuitry. Since this system is designed for low-power operation, it is crucial to select ICs that have low current draw. Table 8 outlines the quiescent current drawn by all of the analog circuitry. The full RTD analog circuitry schematic is shown in Appendix B.

## *3.5 Embedded Processing*

The use of an embedded processor is critical for achieving low-power operation in a small form factor. Known also as a microprocessor, this digital integrated circuit

**Table 8:** Total Quiescent Current Consumption of RTD Analog Circuitry - based on data provided by [45, 46, 48].

| Part | Quantity | Total Quiescent Current Draw |
|---|---|---|
| INA118 | 2 | 700$\mu$A |
| LMC6462 | 4 | 80$\mu$A |
| REF1933 | 1 | 360$\mu$A |
| Voltage Divider ($V_{ref}$) | 1 | 143$\mu$A |
| Howland Pump | 2 | 4mA |
| **Total Current Draw** | - | **5.283mA** |

acts as the brain for the whole operation. It incorporates a central processing unit (CPU) and can process binary register data, read or write to memory, do arithmetic calculations, and much more. Microprocessors are programmed in Embedded C that is tailored to the processor architecture, though its syntax is nearly identical to C.

This system uses an 8-bit microprocessor called ATmega1284P, part of the megaAVR family of processors by Atmel. This microprocessor offers a taste of almost all of the functionality needed for an embedded systems design: flash memory, EEPROM, SRAM, GPIOs, USART, ADC, SPI, I2C, and more. The ATmega1284P can achieve a maximum of 1MIPS per MHz, operating at as low as 1.8V with 0.4mA active current consumption. Even better, the low-power modes of the processor can bring the current consumption down all the way to 0.1$\mu$A during sleep.

There is no non-volatile memory on most microprocessors, hence a memory storage device is required for long term storage without being powered. This system uses a Secure Digital (SD) card for its data storage. SD cards have an optimal form factor and a reduced number of system requirements to be integrated into a low power embedded system. They also are relatively simple to program as long as the file system is understood. By using FatFS, a generic FAT file system for embedded systems, a majority of the software heavy lifting is taken care of by a few API calls, for example to read from or write to storage.

**Table 9:** Total Current Consumption of Embedded Processing Subsection - based on data provided by [2, 5, 41].

| Part | Total Current Consumption |
|---|---|
| ATmega1284P | 0.4mA |
| MicroSD-HC | 70mA |
| BC118 | 16mA |
| **Total Current Draw** | **86.4mA** |

However, a wireless module is required to truly untether the system and allow custom alerts to be made from the device alerting medical staff of any symptoms. Bluetooth Low Energy (BLE) is a relatively new standard of classic bluetooth that offers all of the range and data speeds as previously achieved, but all while consuming a fraction of the power. The BC118 designed by Blue Creation is an ultra low power BLE module that is designed to be used with embedded devices. It offers multiple throughput data rates, including 115200 bits per second mode used by the system, and consumes 16mA of current during communication.

Table 9 shows the total current consumption of the embedded processing subsection of the automated infiltration detection system. Adding this to the total analog circuitry current consumption in Table 8, the total system current draw is approximately 91.6mA at full processing capability. This power, if provided by a 1000mAh Lithium Polymer based battery, gives the device approximately 10 hours of use per charge, not including the use of sleep mode. This extremely low power system architecture is the core behind the automated detection of IV infiltration. Table 10 contains the cumulative measured electrical specifications from the IV2 PCB in Figure 6.

**Table 10:** Electrical Specifications for the IV2 Printed Circuit Board

| **Parameter** | **Typical** | **Unit** |
|---|---|---|
| **System Voltage** | 3.7 | V |
| **System Supply Current** | 130 | mA |
| **Bioimpedance Operation** | | |
| Noise | ±0.5 | Ω |
| Resolution | 3 | Ω |
| Dynamic Range | 0 - 2.8 | kΩ |
| Supply Current | 1 | mA |
| **Strain Operation** | | |
| Noise | ±1.22 | ° |
| Resolution | 5 | ° |
| Dynamic Range | -90 - 90 | ° |
| Supply Current | 0.7 | mA |
| **RTD Operation** | | |
| Noise | ±0.25 | °C |
| Resolution | 1.5 | °C |
| Dynamic Range | 0 - 37 | °C |
| Supply Current | 5 | mA |

# CHAPTER IV

# RESULTS

## *4.1 Experiment Analysis*

The automated infiltration detection system was characterized using both human and non-living subjects. Since a venipuncture must be used to test whether an infusion resulting in infiltration can be sensed, any tests requiring a venipuncture were conducted using a cut of pork belly. Pork belly has multiple layers of connective tissue and fats, and also has a roughly textured top layer similar to skin. Most importantly, this specific cut of pork was chosen because it possesses the physical dimensions of a neonatal arm (Fig. 48). By using pork belly, the system can be characterized using a model extremely close to a neonate's arm while also providing a soft tissue medium for venipuncture.

A saline solution was prepared using formulas described in Chapter 2.1. Saline solution possess a higher conductivity than water due to its high sodium chloride content. Using a high conductivity solution can change the measured biosignals significantly, especially bioimpedance. Finally, the solution was administered using a syringe and 22 gage needle, which most closely matches a neonate's superficial dorsal vein diameter (Fig. 49).

Bioimpedance was measured by using 3M Red Dot Ag/AgCl electrodes in a tetrapolar configuration (Fig. 50). A conductive liquid injected into tissue results in a decrease in bioimpedance, since the liquid content allows for charge to travel more freely through the medium. Figure 51 shows the bioimpedance measurements taken during an infusion test. The impedance of the pork belly pre-infusion rests around 815$\Omega$, with slight variation due to the pre-existing liquid content. The infusion of

saline solution at $t = 22s$ results in a temporary increase in negative slope, followed by a large increase in impedance during the removal of the needle. The bioimpedance post-infusion settles at around $820\Omega$, with a total $\Delta Z = 20\Omega$.

Strain was measured by using strain gages in a Wheatstone bridge configuration. The placement of these gages is extremely important to ensure measurement in the same axial direction across all the sensors. Hence, each gage was placed and fixated very carefully (Fig. 52). The results from the infusion showed the tissue expansion in the localized area as an increasing percent change between $t = 5s$ and $t = 15s$. The percent change measurement clearly defines when an expansion or contraction occurs due to its reference to resting strain, and this makes it extremely easy to identify the modality. Since the pork belly is not contained in skin, the infused liquid leaks out as fast as it is infused, hence the declining slope in percent change post-infusion (Fig. 53).

Surface temperature was measured by using an experimental and control RTD, one at the site of infiltration and the other away from the site of infusion (Fig.54). Still however, the proximity of both sensors based on the size of pork belly resulted in both the control and experiment changing as the solution was infused. The temperature drop was measured to be approximately $3°C$ over the total infusion time. The experimental RTD had a much larger drop in temperature as the liquid was infused and seeped through the tissue and fat layers, as shown near $t = 25$. This can be more clearly shown in the $\Delta$T plot from Figure 56. However, the sporadic noise present in the signal leads to two insights. First, the infused liquid being at a similar temperature to the meat results in a very small change that does not model the human venous blood very well, since venous blood has a much higher temperature. Also, since the meat is porous and has no skin, gravity forces the injected liquid to leak out of the bottom and sides of the section. Since the RTD sensors are placed on the top of the skin, it is possible that the sensors are not able to read the large change in

temperature continuously during the infusion.

The human test was primarily designed to see how the sensing modalities can influence each other, with clear and known relationships between temperature/bioimpedance and temperature/strain. By using a full-bridge circuit for the strain measurement, all changes in temperature are equally represented over all the gages, hence canceling out any reading errors it may cause. However, this is not the case with bioimpedance. The inverse relationship between bioimpedance and temperature was tested by rapidly cooling a section of skin and measuring its real impedance.

The set-up required use of a frozen ice-pack and electrode cuffs constructed for the patient's arm radius (Fig. 58). The contact between the dry copper electrodes and skin had to be seamless to neglect the resistivity associated with the electrode interface. Hence, a large strip of copper tape was wrapped around the arm and secured using velcro straps (Fig. 59). The impedance change resulting from a sharp decrease in temperature was only about $\pm 1\Omega$ from the resting impedance of the skin section, but it can be well within the range of interest when an infusion of liquid results in a change with the same order of magnitude. This result also confirms the hypothesis of an inverse relationship between skin temperature and bioimpedance.

## *4.2 Measurement Results*

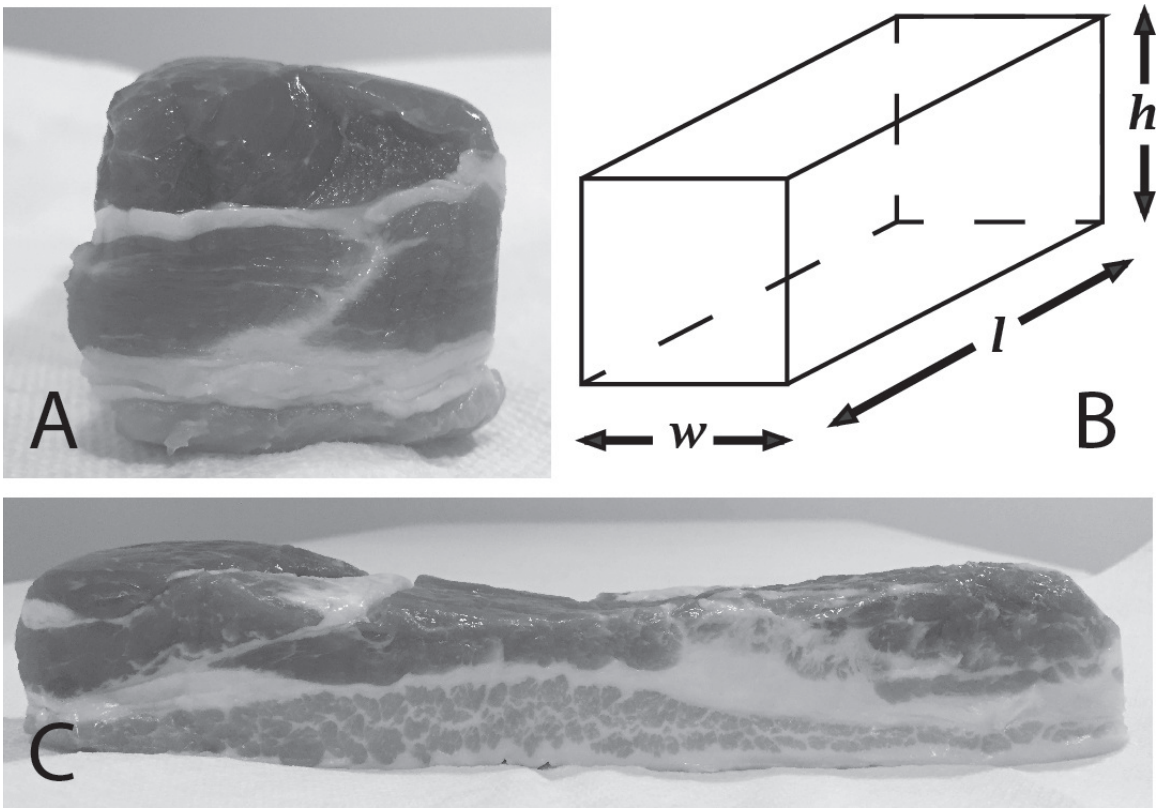


**Figure 48:** Pork belly used for testing automatic infiltration detection sensing modalities. Images showing A) Front-facing view of pork belly with visible layers of fat and subcutaneous tissue B) Pork belly modeled as rectangular prism with $w = 1.25in$, $l = 4.5in$, $h = 1.25in$ C) Cross-section view of pork belly used to model arm.

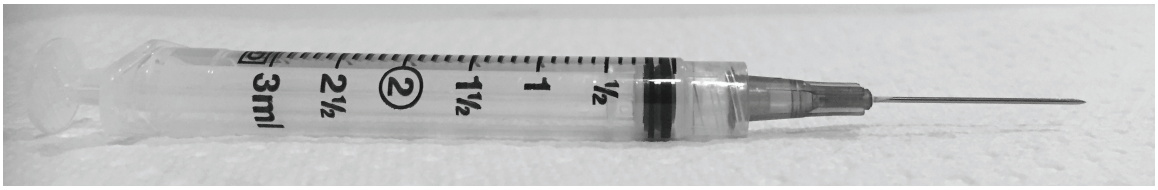


**Figure 49:** Infusion syringe and needle. 3mL of saline was prepared by mixing proportions of water and sodium chloride and administered via a 22 Gage needle tip. The tip was inserted at a 45° angle into the subcutaneous tissue as recommended for intravenous therapy. The solution is brought to room temperature before being slowly injected into the tissue to recreate the intravenous infusion without the use of an angiocatheter or constant drip.

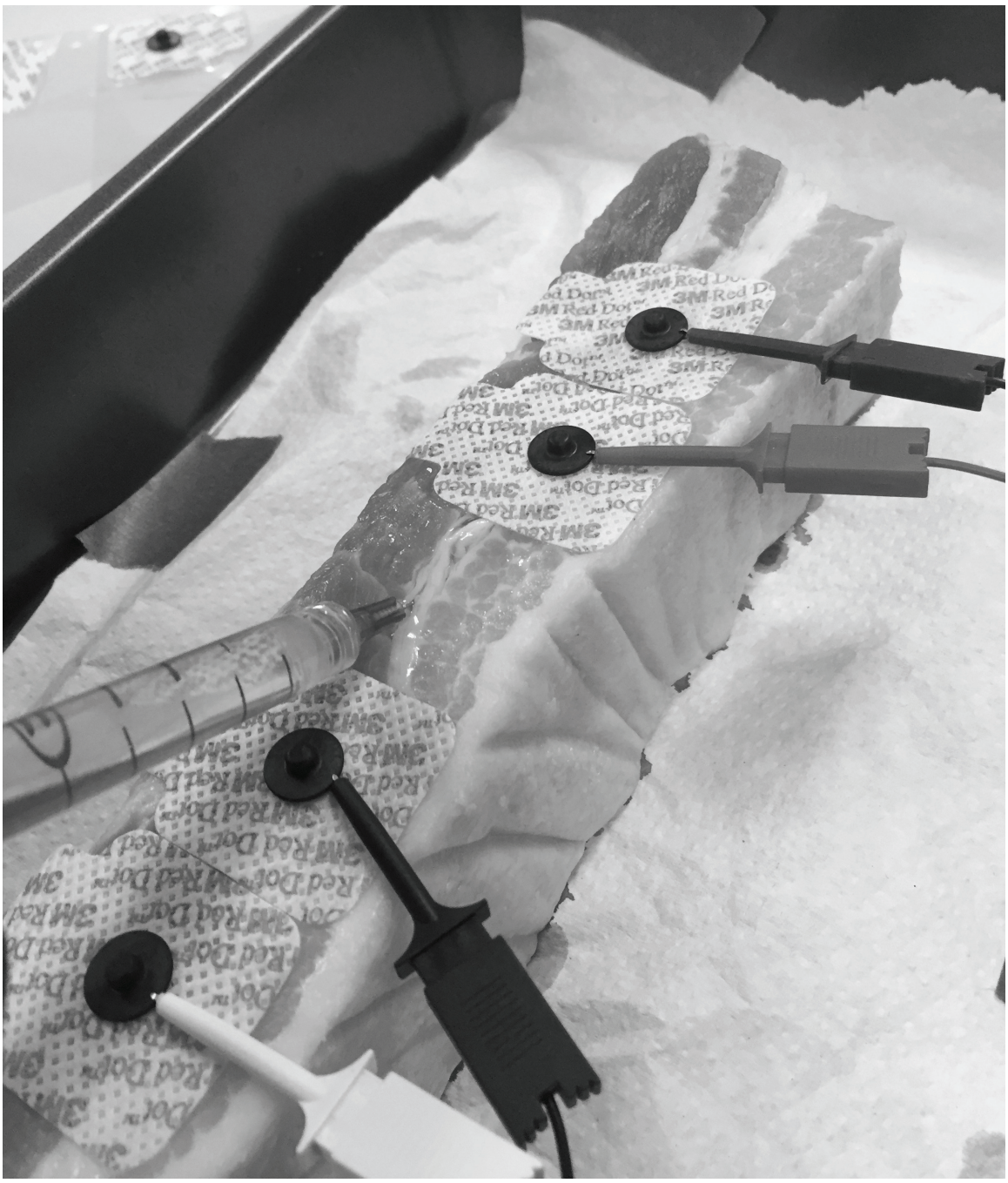

**Figure 50:** Test set-up for measuring bioimpedance across pork belly. This experiment uses 3M Ag/AgCl wet electrodes in a tetrapolar configuration, with spacing between electrodes around the needle site of 0.75 inches. The adhesive material on the electrodes ensured firm contact with the soft tissue.

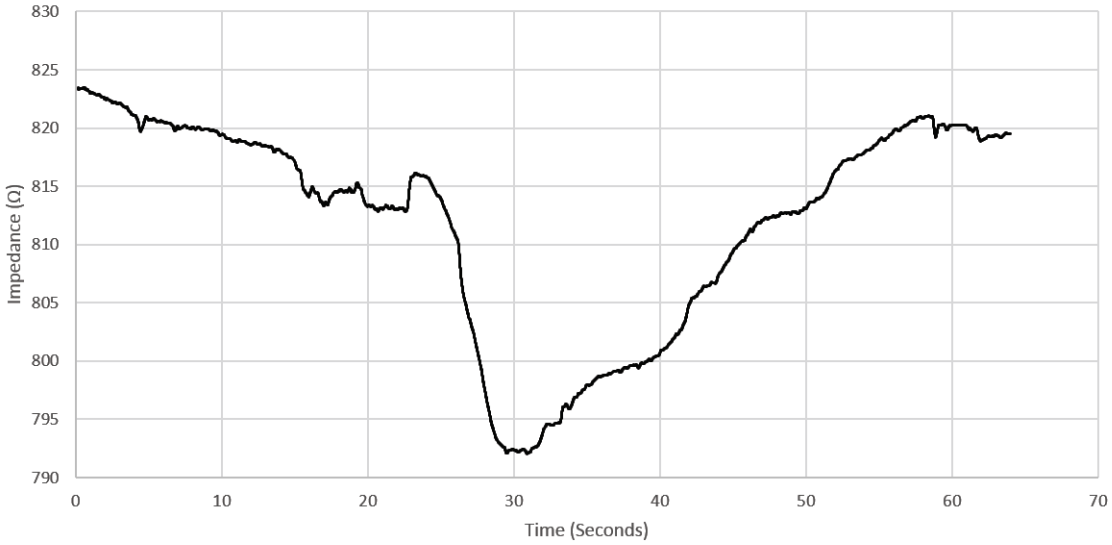


**Figure 51:** Measurement showing change in real ($R_e\{Z\}$) bioimpedance after infusion of nonvesicant saline solution into soft tissue. Infusion of saline solution began at $t = 22s$ and ended at $t = 30s$. The total change in impedance post-infusion is approximately $10\Omega$, which is in line with expected change in bioimpedance with an increase in conductive liquid content. This data was processed in MATLAB with a moving average filter using the vector $y(n) = \frac{1}{20}x(n) + \frac{1}{20}x(n+1) + ... + \frac{1}{20}x(n+19)$.

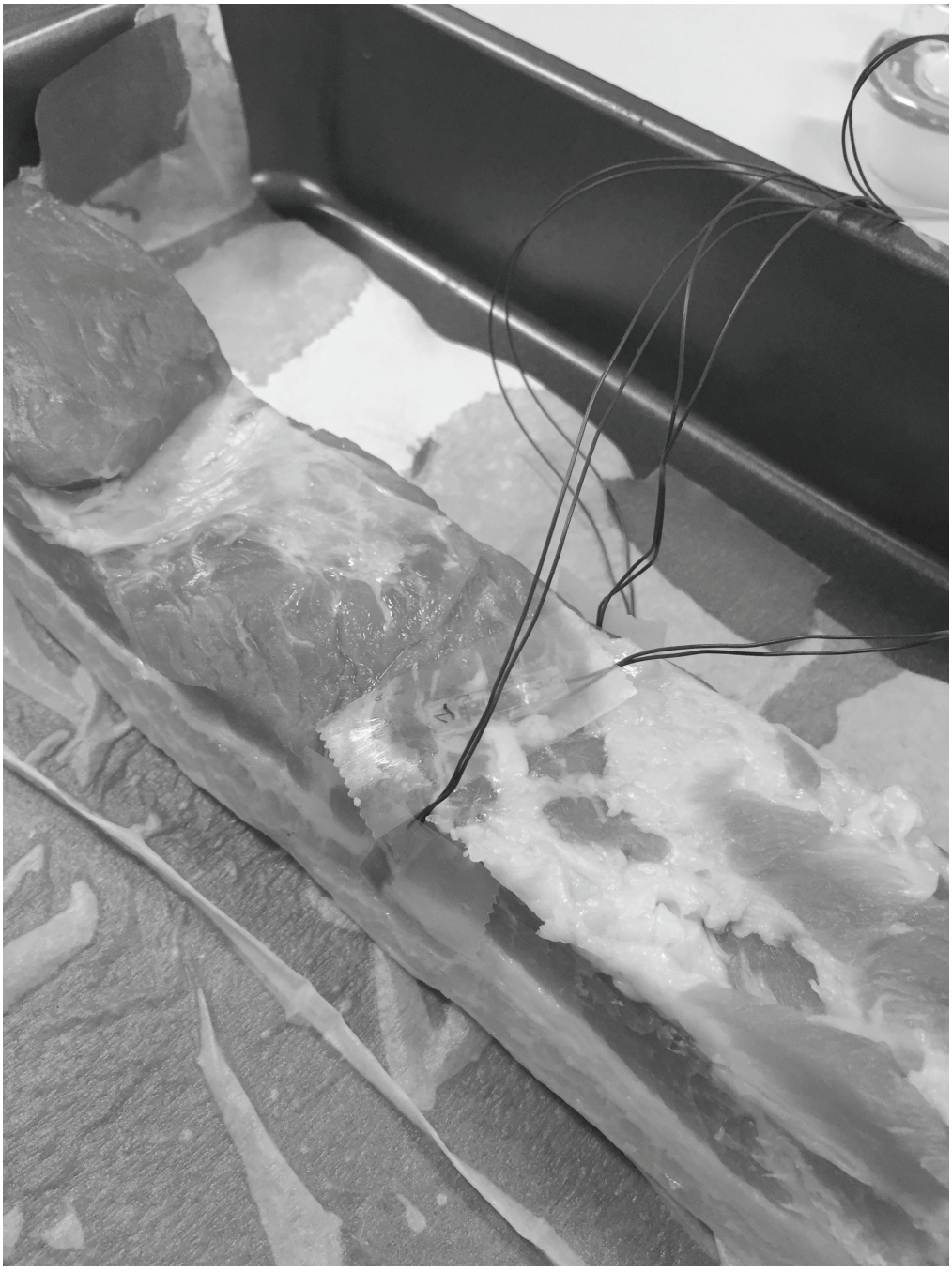

**Figure 52:** Test set-up for measuring strain around pork belly. This experiment uses Omega 120Ω strain gages in a full-bridge Wheatstone configuration. The gages are placed radially to the center of the pork belly to be able to capture swelling in all directions around the skin. Strain gages were placed firmly against the meat and kept in place with an adhesive tape. All gages were placed in the same orientation to ensure that only strain orthogonal to the gage pattern is measured and inflection/deflection are not destructively added together. The needle and syringe were inserted into the center core of the pork belly to measure percent change of tissue expansion with equal bending from each strain gage.

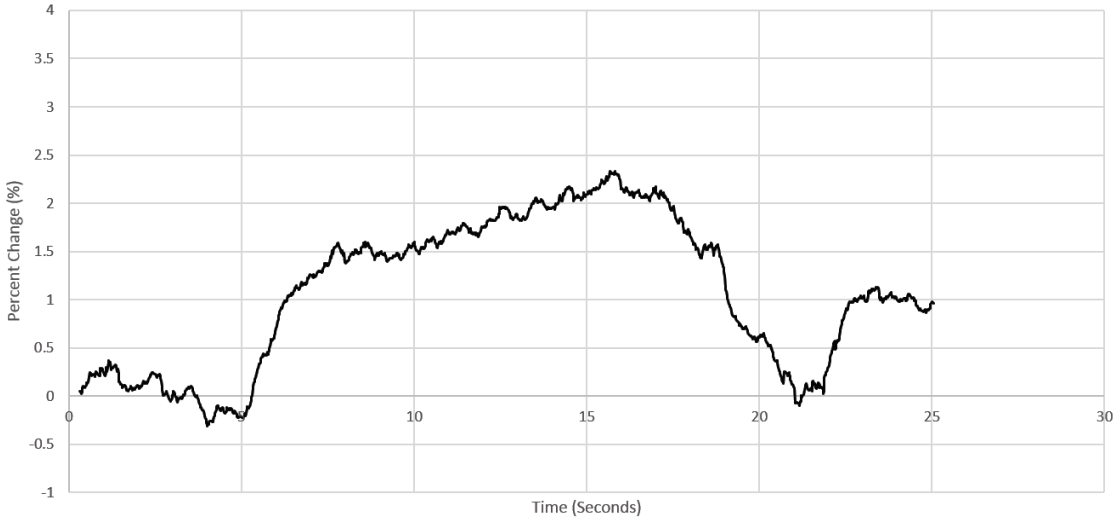


**Figure 53:** Measurement showing percent change in radial strain after infusion of nonvesicant saline solution into soft tissue. Infusion of saline solution began at $t = 5s$ and ended at $t = 15s$. The maximum change is seen at the end of the infusion, reading about 2% expansion of the strain gage bridge. This data was processed in MATLAB with a moving average filter using the vector $y(n) = \frac{1}{20}x(n) + \frac{1}{20}x(n+1) + ... + \frac{1}{20}x(n+19)$.

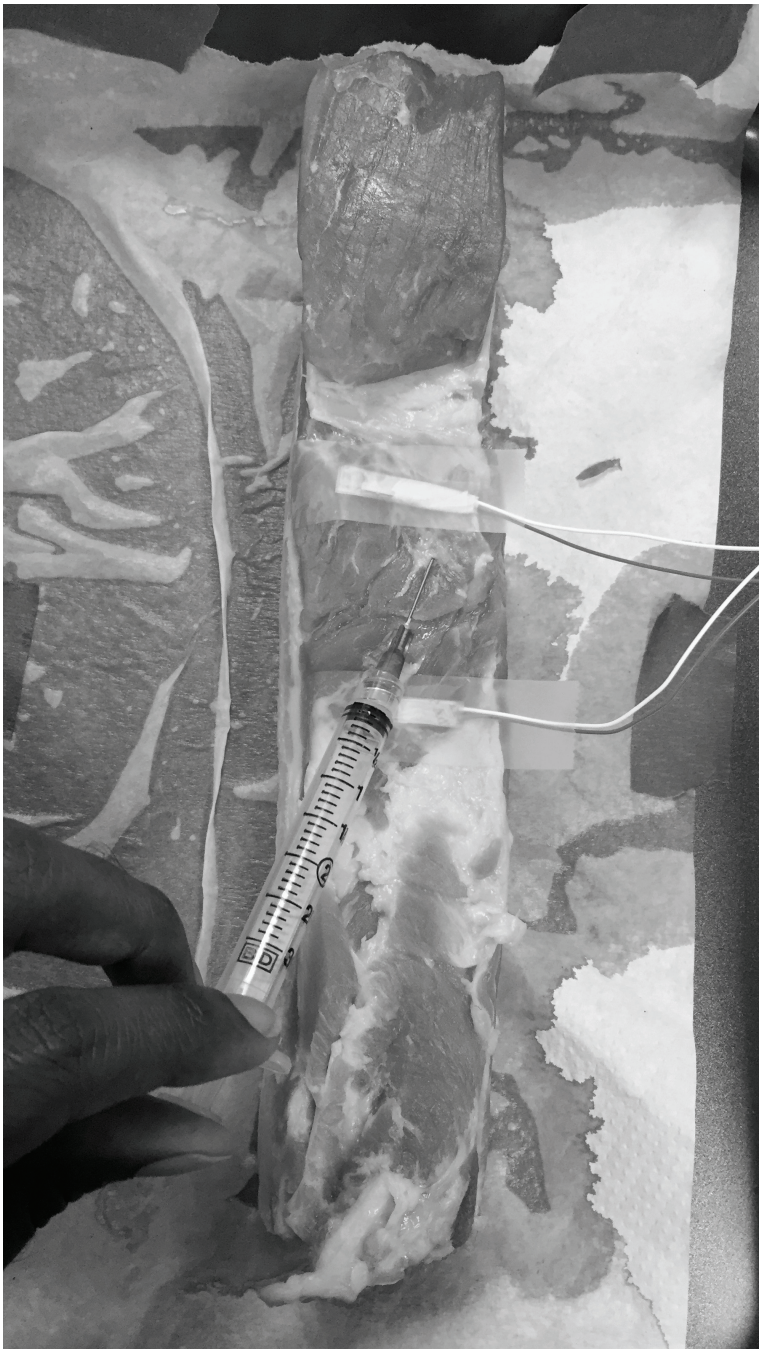

**Figure 54:** Test set-up for measuring temperature on pork belly surface. This experiment uses Measurement Specialties RTD327 sensors in a two-wire configuration. The RTD's are placed 0.5 inches apart, with the experimental sensor being above the infusion site and the control sensor being away from the infusion site. They are mounted using a silicone cover with adhesive backing, with extra adhesive tape being used to ensure placement fixation. The saline solution is released into the tissue below the experimental sensor. For this experiment, the saline solution was kept chilled at $0°C$.

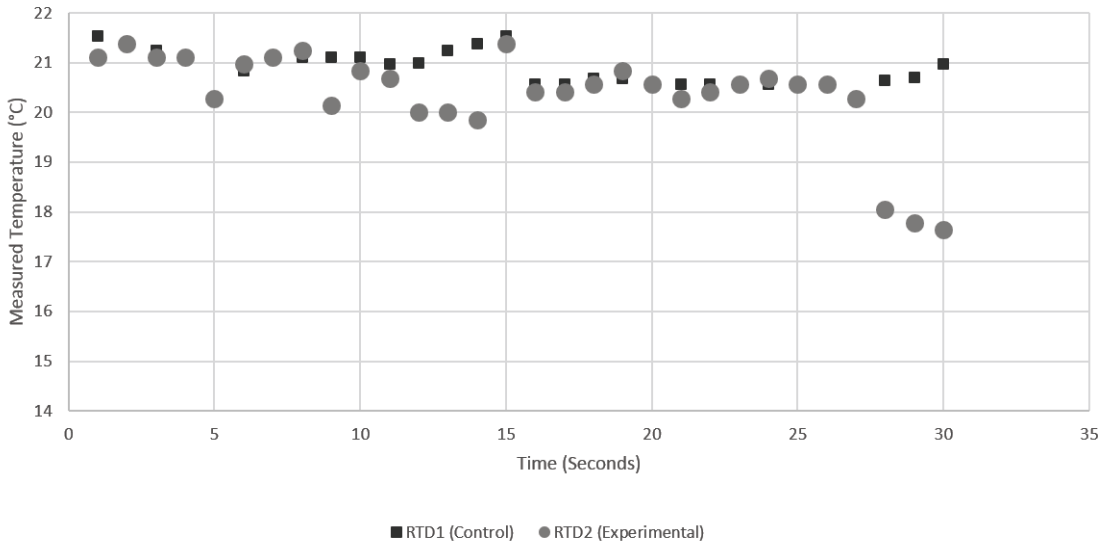


**Figure 55:** Measurement showing the change in temperature for both control and experimental sites. The total change in temperature pre-infustion to post-infusion is 3°C. The experimental sensor results shows declining trend in surface temperature. Infusion of saline solution began at $t = 1s$ and ended at $t = 15s$. The signal noise in between the ends can be attributed to the liquid injected into the meat leaking out through the sides and bottoms and the temperature change not affecting the top of the meat section where the RTD sensors are placed.

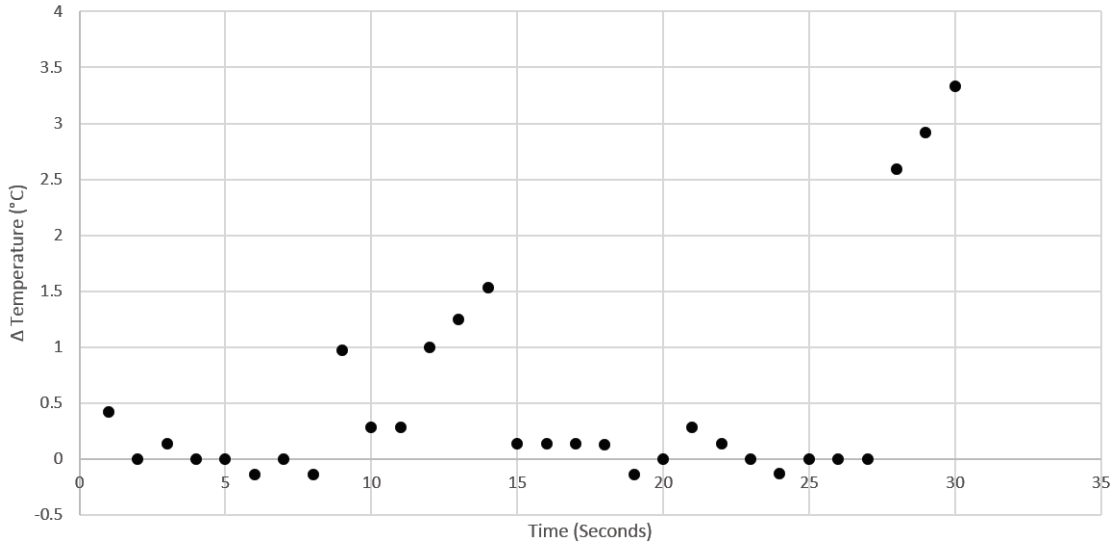


**Figure 56:** Measurement showing the difference ($\Delta = T_{experimental}(^{\circ}C) - T_{control}(^{\circ}C)$) in readings from both sensor sites. Infusion of saline solution began at $t = 5s$ and ended at $t = 15s$. The large change in temperature is detected by the experimental RTD sensor at $t = 27s$.

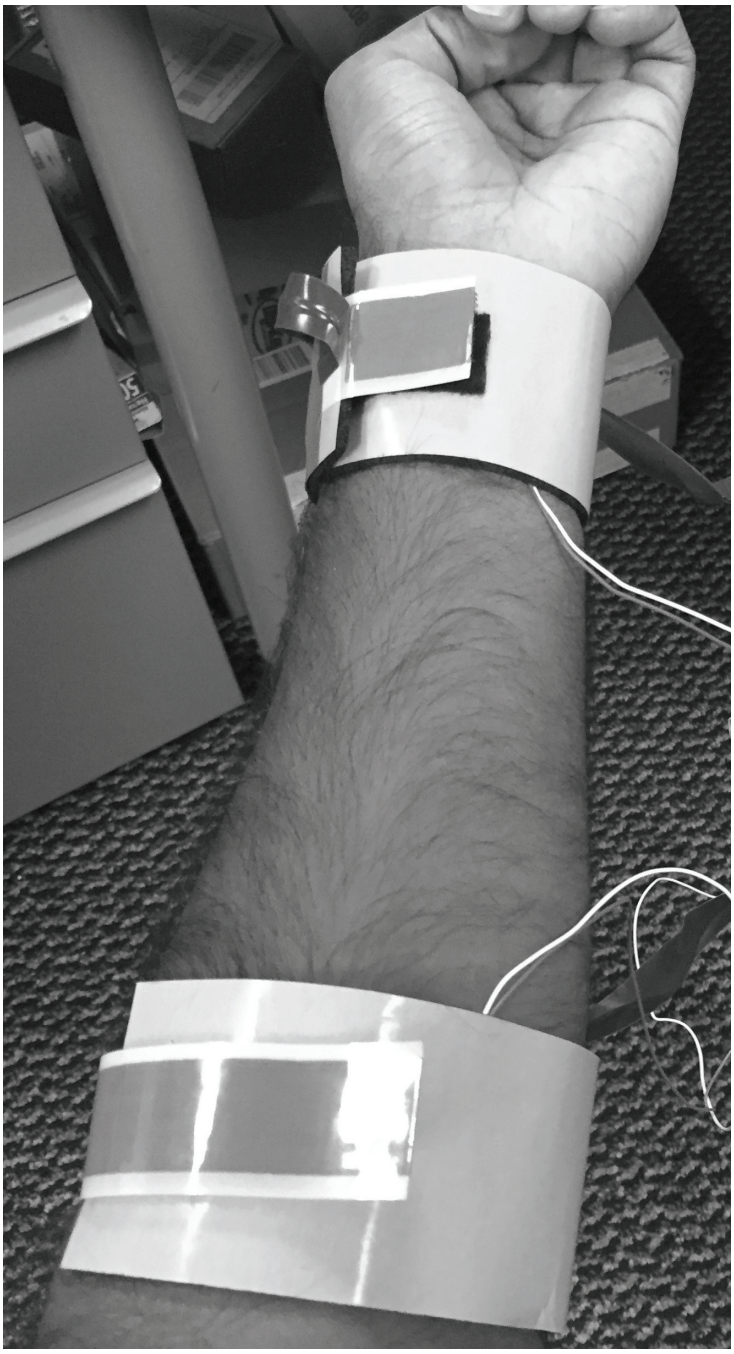

**Figure 57:** IRB approved human trial used to characterize sensing modalities without puncturing the skin. Electrode cuffs mounted on either side of typical IV catheter sites and configured for tetrapolar measurements. Cuffs are secured on arm with velcro straps, meant to ensure maximum skin-electrode contact.

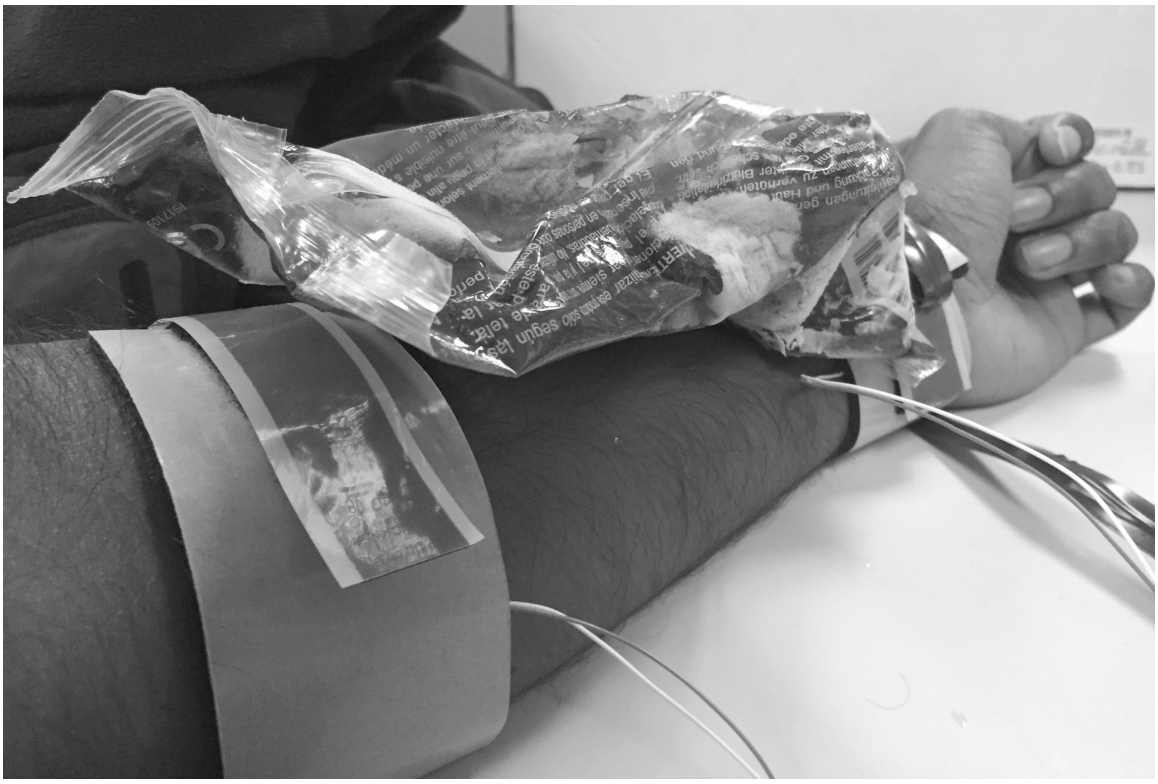

**Figure 58:** Test set-up for measuring bioimpedance on human subject. This experiment uses custom-made dry electrode cuffs. The cuffs are placed 3 inches apart to see the effect of chilling the maximum surface area of the arm. A near-frozen ice pack is used to rapidly cool the site.

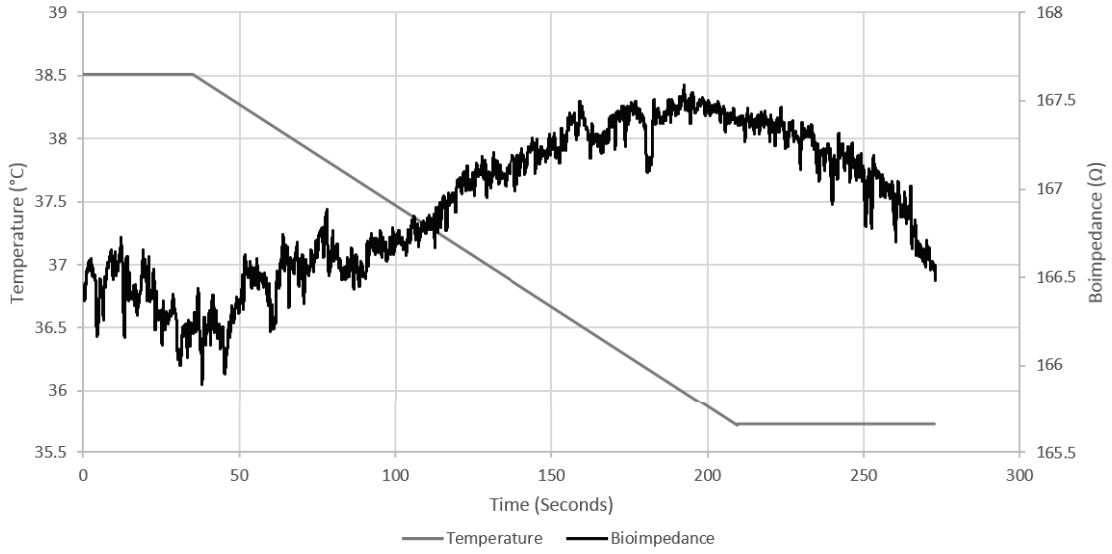


**Figure 59:** Measurement showing the change in bioimpedance at site in-between electrode cuffs based on the rapid change in skin temperature plotted against a linear extrapolation of skin temperature based on recordings from the beginning and end of the experiment. The ice pack is placed on the skin at $t = 40s$ and removed at $t = 210s$. The inverse relationship between skin temperature and bioimpedance is seen within this timeframe. The bioimpedance data was processed in MATLAB with a moving average filter using the vector $y(n) = \frac{1}{20}x(n) + \frac{1}{20}x(n+1) + ... + \frac{1}{20}x(n+19)$.

# CHAPTER V

# DISCUSSION

The experiments conducted to measure the physiological response to a liquid leakage in soft tissue were key to better designing the system, as there are were direct correlations and a few limitations that were discovered. While individual modality characterization could be done relatively easily, either by using phantom loads for bioimpedance or measuring fixed temperature solutions for RTD performance, it was challenging to devise a comprehensive test that attempted to capture liquid leakage.

The pork belly test was designed to emulate the neonatal arm, in the hopes that it reveals similar characteristics as what were expected from a real patient. The infusion of saline via 22 gage needle and syringe was essential to validating the experiment, as these items are the same equipment used for IV therapy in a hospital setting. The physiological responses elicited from these tests were compared to the original hypothesis for the modality, and the positive results from these tests lead this research to further invest in these sensing modalities.

The bioimpedance results were positive in reacting to a liquid infusion by reducing the impedance seen. The physiological range noticed through this experiment was -20Ω change after infusing 3mL of conductive solution, from a pre-infusion resistance of 815Ω. This is a very detectable change by the system, and can conclusively measure whether liquid content around the electrodes has changed by a few milliliters. The bounce back to pre-infusion resistance level in approximately 30 seconds was unexpected, but shows that the liquid content reduces as it leaks out of the meat. Since there is no skin surrounding the meat, it does not stay in the local area. The types of electrodes used for measurement must also be further characterized to make

conclusive statements about the fixed impedance of a section of pork belly, which can change any percent change measurements used for infiltration notification thresholds.

The strain results were also positive in reacting to liquid infusion. The 2% change indicates an expansion of the pork belly after the 3mL infusion of saline. The pull-back seen post infusion was also seen and in line with the same response elicited in the bioimpedance tests. Though the start of an infiltration can be detected via the rise or falls in these physiological measurements, the pullback after infusion has ceased is seen to be extremely important to measure as well. These sections can also give medical staff insightful information on how much liquid has leaked and the exact timing associated. There are a few improvements that can be made after attempting this experiment.Though this test is should be independent of the type of solution infused, it would be beneficial to test other types liquids to validate this hypothesis. Also, the mounting of strain gages on the meat in a Full-bridge Wheatstone configuration was a significant challenge when conducting this test, and devising a better gage placement technique would greatly improve the results seen.

The temperature measurements were able to detect the drop in temperature post-infusion, but were the poorest results out of the three pork belly experiments conducted. The distance between the control and experimental sensors was too small to be able to measure a change in differential temperature. The placement of the control RTD must be further investigated to act independent from any infusions taking place. The sporadic signal obtained makes it challenging to conclusively determine whether an infiltration has occurred. While reducing the sampling rate of the RTD circuitry is an option, it is also possible that measuring skin temperature is a slower detectable response to infiltration. The time it takes for the temperature drop to permeate from the inner soft tissue all the way to the surface is significantly higher than expected. Also, since there is no skin surrounding the pork belly, it is possible that all of the liquid rapidly leaked out of the section without affecting the RTDs, which were placed

on the top of section near the infusion site.

Finally, the human bioimpedance measurement fell in line with the hypothesis presented between temperature change and bioimpedance change. Their inverse relationship was clearly detected, but the magnitude of change was much smaller than expected. However, the $\pm 1\Omega$ change in bioimpedance presented by the rapid cooling of the skin is a significant response to take into consideration, because this must be used to calibrate the measurement readings taken from the bioimpedance front end. The system will need to be able to calculate the temperature change and correct for this in the bioimpedance measurement results.

The pork belly and human experiments were able to help understand the physiological changes associated with IV infiltration. The success of the bioimpedance, strain, and bioimpedance/temperature measurements are key takeaways for improving the testing and further instrumentation design of the system. Equally important is the challenge presented by measuring surface temperature using the RTD pair. This sensing modality, though expected to be one of the first symptoms detectable, is more challenging to use as an indicator of IV infiltration. However, further improving the testing methods used can possibly render this measurement more responsive and useful.

# CHAPTER VI

# CONCLUSION

The popularity of intravenous therapy for administering medications lies in stark contrast with the technology available to ensure its long-term effectiveness. With over 30% of IV catheters failing during their specified duration, many hospital-associated complications stem from improper monitoring of the catheter site. NICU's pose an even greater challenge for monitoring IV catheters, due to the patients smaller venous system and inability to communicate with medical staff. For these reasons, and many more, a system must be designed to monitor IV catheter sites for any infiltrations amongst neonates.

This thesis proposes a novel automated detection system based on high-resolution, wireless, non-invasive sensing of bioimpedance, strain, and temperature around the catheter site. By combining state-of-the-art sensors with a low power embedded processing unit, this device could be mechanically designed to sit around the catheter site for long periods of time without impeding the neonate's mobility. The availability of low-cost sensors and microprocessors make this solution economically feasible for all types of medical care, not limited only to NICUs.

The rigorous characterization of the non-invasive sensing modalities undertaken is meant to help grasp an understanding of what type of physiological ranges are associated with IV infiltration. By testing the modalities against their real world equivalences and successively emulating their operation on soft tissue similar to a neonatal arm, the system's proof of concept illustrates that this scheme can be used to automatically detect IV infiltration. Finally, bringing upon an understanding of the physiological cross-talk associated with taking measurements from a human subject

gives the system a redundant understanding of the biosignals it is sensing.

The future for this kind of sensing system is bright. Working out the digital signal processing and wireless communication protocols for achieving real-time alerts based on characterized thresholds are the immediate goals in sight. But there is much more that can be done by a system as such to improve the quality of care in Neonatal Intensive Care Units. Miniaturizing the device for comfortable long-term wear is crucial to widespread adoption of intravenous monitoring, as well as reducing the cost by further optimizing the system architecture.

With all of the ground work done in this thesis, a non-invasive automatic intravenous infiltration detection system for use amongst neonates is something that is truly achievable, and achievable soon. This thesis aims to provide a platform by which future researchers can begin to apply the concepts presented here to begin to save neonatal lives. Though it might be difficult to realize the scale by which a system as such can save these lives, discussing and working towards this goal is imperative to improving the quality of care for our most precious patients.

# APPENDIX A

# FIGURES AND TABLES

**Table 11:** Average Daily TPN Micronutrient Composition - based on data provided by [19]

| **Micronutrient** | **Quantity** |
|---|---|
| Vitamin A | 3300 IU |
| Vitamin D | 200 IU |
| Vitamin E | 10 IU |
| Thiamine (B-1) | 6 mg |
| Riboflavin (B-2) | 3.6 mg |
| Niacin (B-3) | 40 mg |
| Pantothenic acid (B-5) | 15 mg |
| Pyridoxine (B-6) | 4 mg |
| Biotin (B-7) | 60 g |
| Folic acid (B-9) | 600 g |
| Cobalamin (B-12) | 5 g |
| Vitamin C | 200 mg |
| **Trace Elements** | |
| Zinc | 5 mg |
| Copper | 1 mg |
| Chromium | 10 g |
| Manganese | 0.5 g |
| Selenium | 60 g |
| **Electrolytes** | |
| Sodium | 60150 mEq |
| Potassium | 40100 mEq |
| Chloride | 60150 mEq |
| Magnesium | 16 mEq |
| Phosphorus | 1030 mmol |
| Calcium | 10 mEq |

**Table 12:** Most Commonly Reported Medications in NICU's - based on data provided by [9]

| **Medication** | **Frequency** |
|---|---|
| Ampicillin | 186,799 |
| Gentamicin | 171,388 |
| Ferrous Sulfate | 90,152 |
| Vitamin (multivitamin) | 64,329 |
| Cefotaxime | 55,455 |
| Caffeine citrate | 48,814 |
| Furosemide | 47,278 |
| Vancomycin | 44,218 |
| Beractant | 36,410 |
| Dopamine | 25,839 |
| Nystatin | 24,323 |
| Normal Saline | 24,063 |
| Ranitidine | 23,905 |
| Indomethacin (Ibuprofen) | 20,605 |
| Dexmethasone | 20,398 |
| Albuterol | 18,767 |
| Fentanyl | 18,648 |
| Phenobarbital | 17,363 |
| Sodium Bicarbonate | 16,291 |
| Calafactant | 15,676 |
| Sodium Chloride | 15,602 |
| Epoetin-$\alpha$ | 14,676 |
| Morphine | 11,646 |
| Midazolam | 11,634 |
| Erythromycin | 10,748 |
| Tobramycin | 10,495 |
| Glycerin | 9,987 |
| Oil | 9,795 |

# APPENDIX B

# CUSTOM ELECTRONICS SCHEMATIC AND LAYOUT

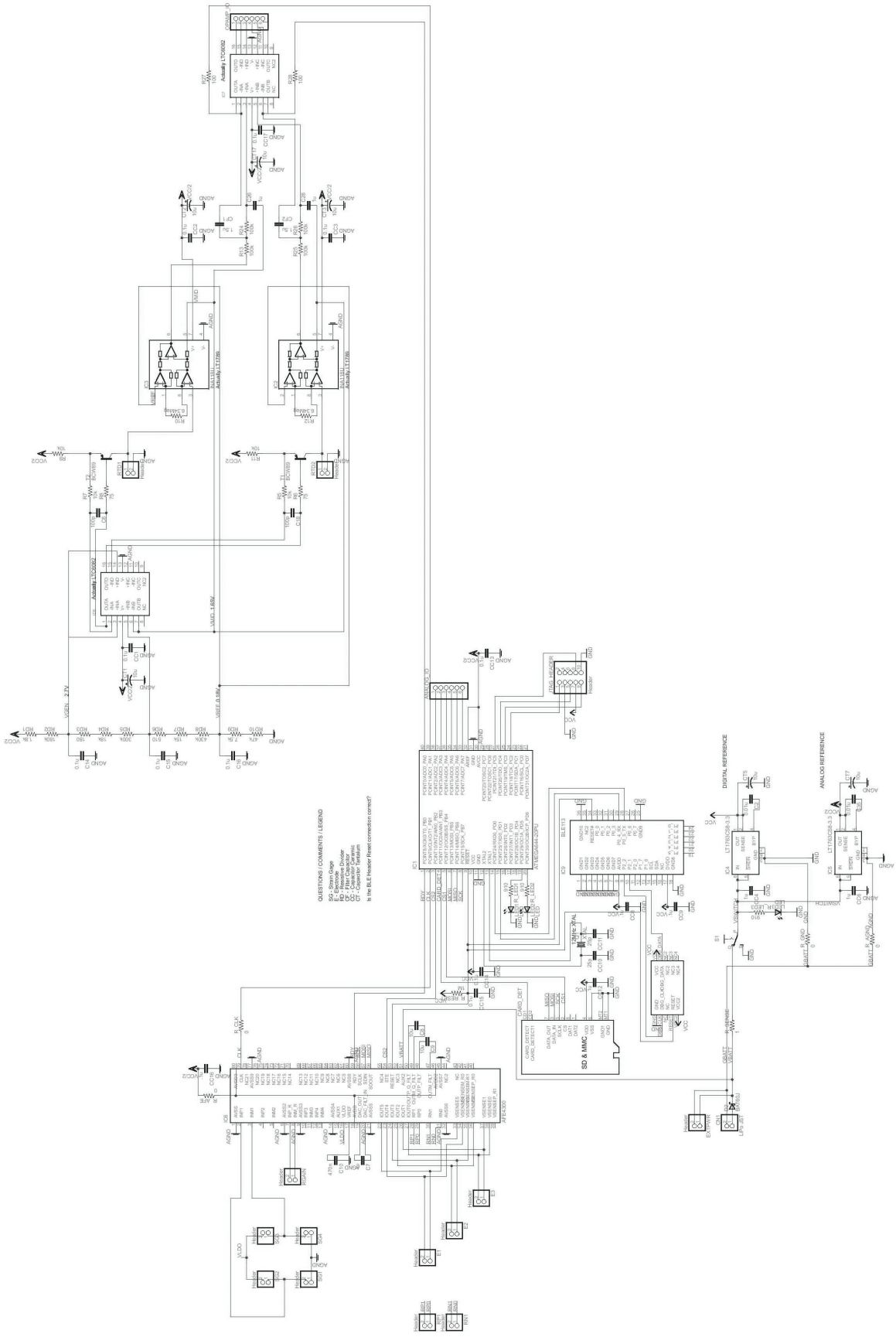

**Figure 60:** Schematic for IV Rev 1 Printed Circuit Board, made with EAGLE V7.2.0

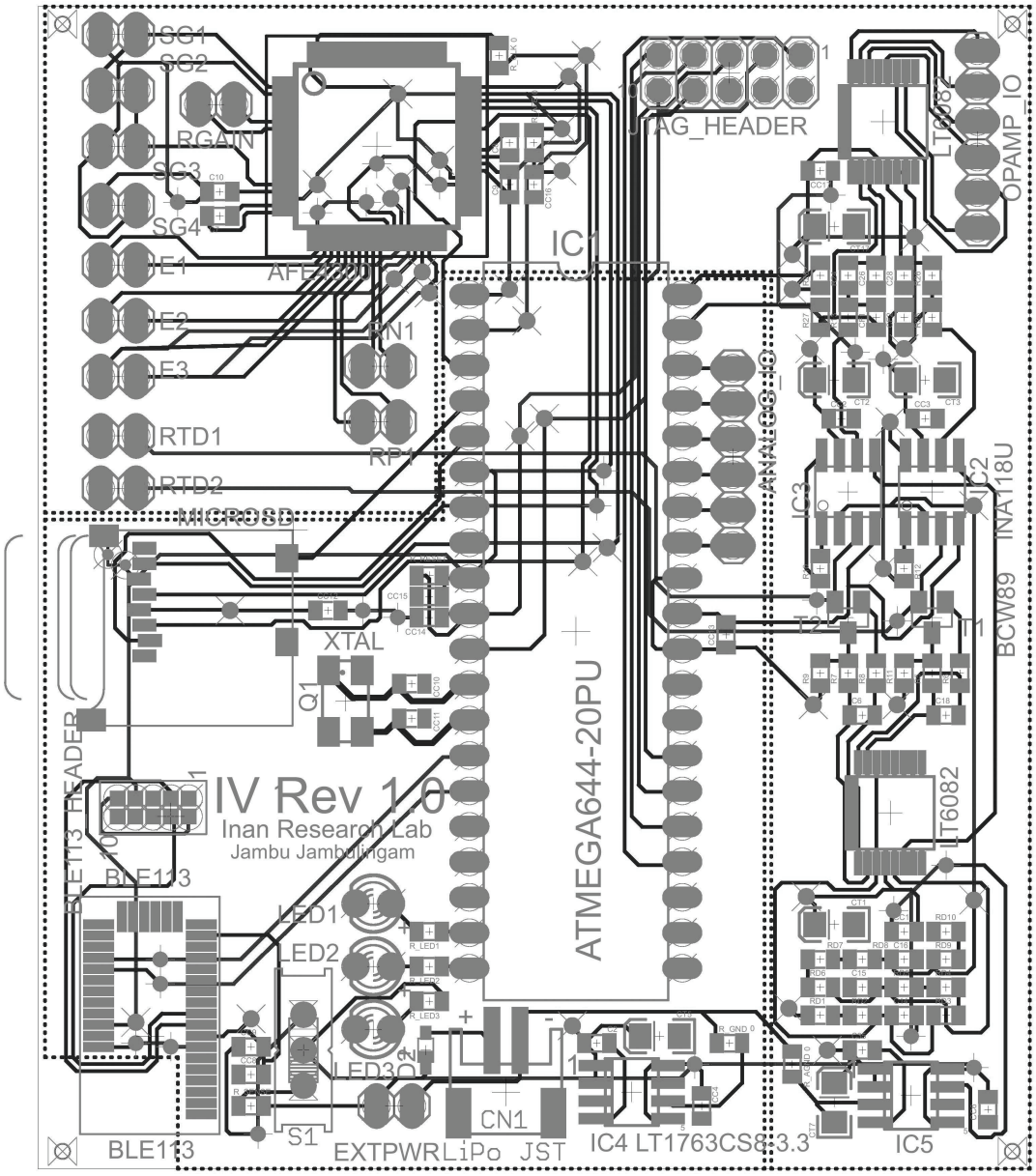


**Figure 61:** Layout for IV Rev 1 Printed Circuit Board, made with EAGLE V7.2.0

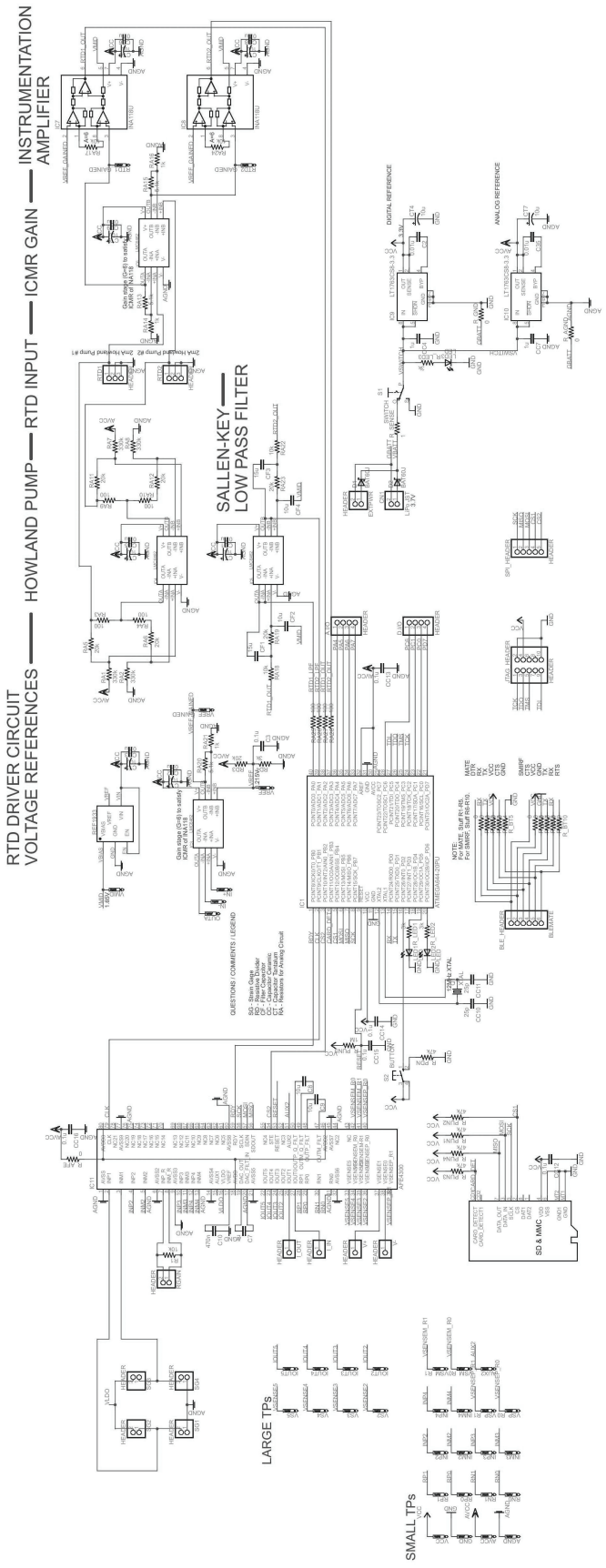


**Figure 62:** Schematic for IV Rev 2 Printed Circuit Board, made with EAGLE V7.2.0

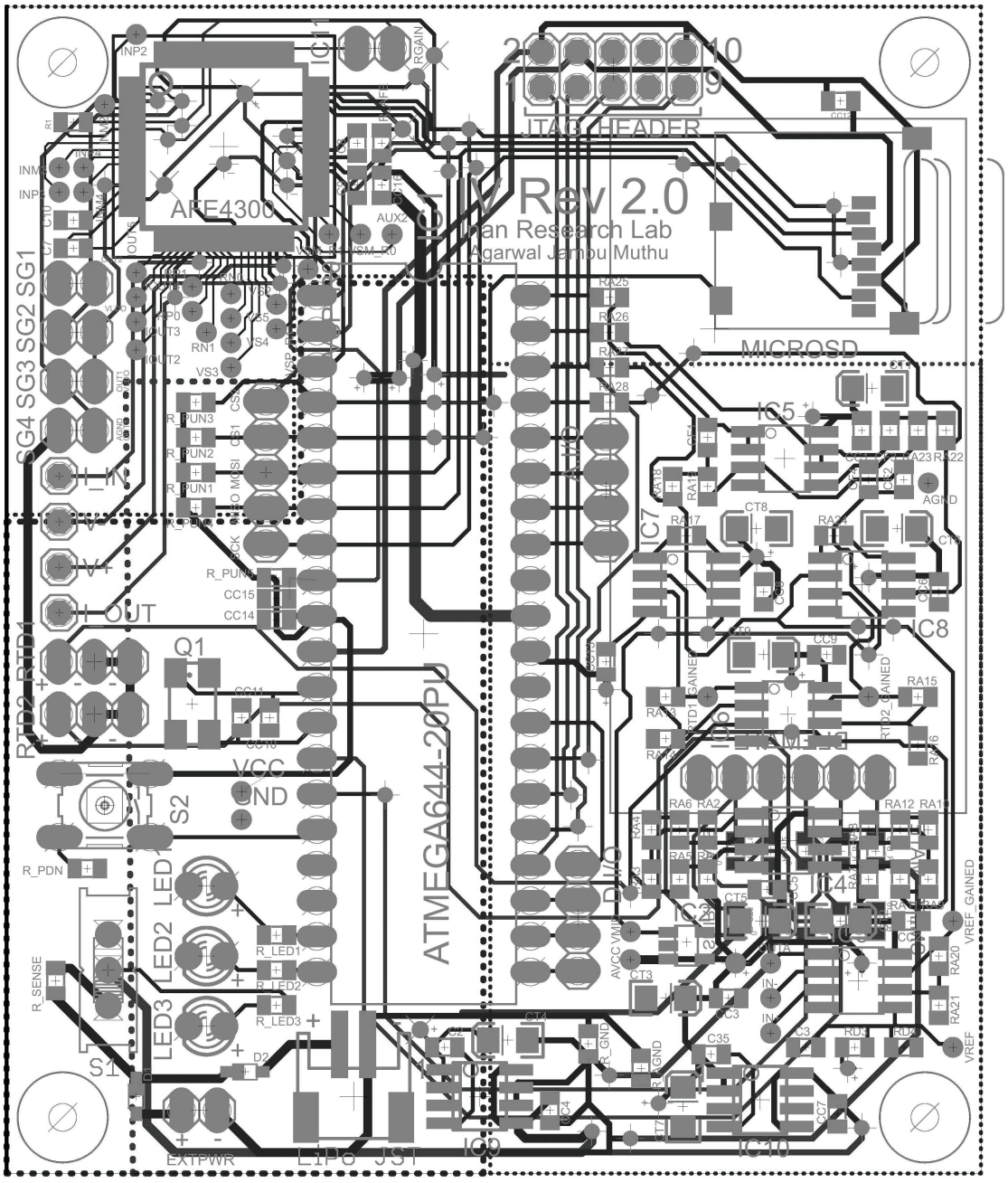


**Figure 63:** Layout for IV Rev 2 Printed Circuit Board, made with EAGLE V7.2.0

# REFERENCES


[1] Amano, H., Nagai, Y., Kowase, T., and Ishikawa, O., "Cutaneous necrosis induced by extravasation of arginine monohydrochloride," *Acta dermato-venereologica*, vol. 88, no. 3, pp. 310–311, 2008.

[2] Atmel, *8-bit AVR Microcontroller with 128K Bytes In-System Programmable Flash*, 12 2009. Rev. D.

[3] Bartels, K., Moss, D. R., and Peterfreund, R. A., "An analysis of drug delivery dynamics via a pediatric central venous infusion system: quantification of delays in achieving intended doses," *Anesthesia & Analgesia*, vol. 109, no. 4, pp. 1156–1161, 2009.

[4] Binette, J., Garon, M., Savard, P., McKee, M., and Buschmann, M., "Tetrapolar measurement of electrical conductivity and thickness of articular cartilage," *Journal of biomechanical engineering*, vol. 126, no. 4, pp. 475–484, 2004.

[5] Blue Creation, *BC118 Datasheet*, 11 2015. Rev. A.

[6] Capraro, A. M., Weiner, Debra MD, P., and Morin, Michele RN, N., *Intravenous Catheter Placement*.

[7] Carson, D. and Dychter, S. S., "Intravenous therapy: A review of complications and economic considerations of peripheral access," *Heart Failure*, 2011.

[8] Chi, Y. M., Jung, T.-P., and Cauwenberghs, G., "Dry-contact and non-contact biopotential electrodes: methodological review," *Biomedical Engineering, IEEE Reviews in*, vol. 3, pp. 106–119, 2010.

[9] Clark, R. H., Bloom, B. T., Spitzer, A. R., and Gerstmann, D. R., "Reported medication use in the neonatal intensive care unit: data from a large national data set," *Pediatrics*, vol. 117, no. 6, pp. 1979–1987, 2006.

[10] Cleveland Clinic Center for Continuing Education, *Principles of Nutrition Support*, 8 2013.

[11] Columbia University Center for Teaching and Learning, *Medical Emergencies and Complications: IV Complications*.

[12] Commons, W., "Neonatal intensive-care unit in 2009 - gnu free documentation license," 2009.

[13] Commons, W., "Simplified diagram of the human venous system in anterior view. - gnu free documentation license," 2009.

[14] CVS Specialty Infusion Services, *Storage of Total Parenteral Nutrition (TPN)*, 1 2009.

[15] Doellman, D., Hadaway, L., Bowe-Geddes, L. A., Franklin, M., LeDonne, J., Papke-O'Donnell, L., Pettit, J., Schulmeister, L., and Stranz, M., "Infiltration and extravasation: update on prevention and management," *Journal of Infusion Nursing*, vol. 32, no. 4, pp. 203–211, 2009.

[16] Dusen, M. V., "Platinum-resistance thermometry at low temperatures1," *Journal of the American Chemical Society*, vol. 47, no. 2, pp. 326–332, 1925.

[17] Frank, Robert L MD, F., *UpToDate*. UpToDate, 2015.

[18] Hadaway, L., "Emergency: Infiltration and extravasation," *The American Journal of Nursing*, vol. 107, no. 8, pp. 64–72, 2007.

[19] Halter, J., Ouslander, J., Tinetti, M., Studenski, S., High, K., and Asthana, S., *Hazzard's Geriatric Medicine and Gerontology, 6e*. McGraw-Hill, 2009.

[20] Helm, R. E., Klausner, J. D., Klemperer, J. D., Flint, L. M., and Huang, E., "Accepted but unacceptable: Peripheral iv catheter failure," *Journal of Infusion Nursing*, vol. 38, no. 3, pp. 189–203, 2015.

[21] Honeywell, *Platinum RTD Resistance vs. Temperature Function*, 5 2014.

[22] Humphrey, J. D. and DeLange, S., *An introduction to biomechanics: solids and fluids, analysis and design*. Springer Science & Business Media, 2013.

[23] Intravenous Nursing New Zealand, *Intravenous Therapy: Then and Now*, 7 2013.

[24] Khalil, S. F., Mohktar, M. S., and Ibrahim, F., "The theory and fundamentals of bioimpedance analysis in clinical status monitoring and diagnosis of diseases," *Sensors*, vol. 14, no. 6, pp. 10895–10928, 2014.

[25] Kyle, U. G., Bosaeus, I., De Lorenzo, A. D., Deurenberg, P., Elia, M., Gómez, J. M., Heitmann, B. L., Kent-Smith, L., Melchior, J.-C., Pirlich, M., and others, "Bioelectrical impedance analysispart i: review of principles and methods," *Clinical nutrition*, vol. 23, no. 5, pp. 1226–1243, 2004.

[26] Liu, Y., Wang, L., Liu, J., and Di, Y., "A study of human skin and surface temperatures in stable and unstable thermal environments," *Journal of Thermal Biology*, vol. 38, no. 7, pp. 440–448, 2013.

[27] Magill, S. S., Edwards, J. R., Beldavs, Z. G., Dumyati, G., Janelle, S. J., Kainer, M. A., Lynfield, R., Nadle, J., Neuhauser, M. M., Ray, S. M., and others, "Prevalence of antimicrobial use in us acute care hospitals, may-september 2011," *JAMA*, vol. 312, no. 14, pp. 1438–1446, 2014.

[28] Martinsen, O. G. and Grimnes, S., *Bioimpedance and bioelectricity basics*. Academic press, 2011.

[29] Measurement Specialties, *Polyimide Surface RTD Sensor*, 1 2014. Rev. 1.

[30] Millikan, R. A. and Bishop, E. S., *Elements of electricity: a practical discussion of the fundamental laws and phenomena of electricity and their practical applications in the business and industrial world*. American Technical Society, 1917.

[31] National Instruments, *Strain Gauge Configuration Types*, 8 2006.

[32] National Instruments, *Taking Temperature Measurements with RTDs: How-To Guide*, 11 2014.

[33] NICU-Pedia, *NICU Medications*, 5 2014.

[34] Nybo, L. and Secher, N. H., "Counterpoint: humans do not demonstrate selective brain cooling during hyperthermia," *Journal of Applied Physiology*, vol. 110, no. 2, pp. 571–573, 2011.

[35] OMEGA Engineering, *Precision Strain Gage SGD Series*. Rev. 1.

[36] OSCE Skills, *Intravenous Cannulation - Creative Commons Attribution License*, 1 2015.

[37] Pixabay, "Surgery surgeons operation medical health doctors - creative commons cc0 license," 2015.

[38] Raimondi, A. J., *Pediatric Neurosurgery: Theoretical Principles. Art of Surgical Techniques*. Springer Science & Business Media, 2013.

[39] Roberts, J. R. and Hedges, J. R., *Clinical procedures in emergency medicine*. Elsevier Health Sciences, 2009.

[40] Sadd, M. H., *Elasticity: theory, applications, and numerics*. Academic Press, 2009.

[41] SanDisk, *SanDisk SD Card*, 11 2004. Rev. 2.2.

[42] Simona, R., "A pediatric peripheral intravenous infiltration assessment tool," *Journal of Infusion Nursing*, vol. 35, no. 4, pp. 243–248, 2012.

[43] Sung, C. Y., Chung, R. K., Ra, Y. S., Lee, H. S., and Lee, G. Y., "Impending compartment syndrome of the forearm and hand after a pressurized infusion in a patient under general anesthesia-a case report - creative commons attribution license," *Korean journal of anesthesiology*, vol. 60, no. 1, pp. 60–63, 2011.

[44] Tektronix, *Two-Wire vs. Four-Wire Resistance Measurements: Which Configuration Makes Sense for Your Application?*, 5 2013.

[45] Texas Instruments, *Precision, Low Power Instrumentation Amplifier*, 5 1998. Rev. A.

[46] Texas Instruments, *LMC6462 Dual/LMC6464 Quad Micropower, Rail-to-Rail Input and Output CMOS Operational Amplifier*, 3 2013. Rev. D.

[47] Texas Instruments, *Low-Cost, Integrated Analog Front-End for Weight-Scale and Body Composition Measurement*, 6 2013. Rev. B.

[48] Texas Instruments, *REF19xx Low-Drift, Low-Power, Dual-Output, VREF and VREF/2 Voltage References*, 8 2014. Rev. A.

[49] University of Miami Miller School of Medicine, *Neonatology Clinical Services*.

[50] Webster, J. G., *Medical Devices and Instrumentation*. Wiley-Interscience, 1988.

[51] Widmaier, E., Raff, H., and Strang, K., "Cardiovascular physiology," *Vanders human physiology: The mechanisms of body function*, pp. 386–476, 2006.

[52] Winchester, L. W. and Chou, N.-Y., "Optical detection of intravenous infiltration," in *Biomedical Optics 2006*, pp. 608016–608016, International Society for Optics and Photonics, 2006.